Nanoscale Horizons

REVIEW

View Article Online
View Journal

Cite this: DOI: 10.1039/d5nh00377f

Laser-induced graphene for biomedical applications: innovations in health monitoring and diagnostics

Truong-Son Dinh Le,[a] Y-Van Tran,[ab] Yuji Gao,[c] Von Luigi Valerio,[a] Zhixing Ge[ad] and Chwee Teck Lim *[acde]

Received 30th May 2025,
Accepted 30th July 2025

DOI: 10.1039/d5nh00377f

rsc.li/nanoscale-horizons

Laser-induced graphene (LIG) has emerged as a versatile and sustainable nanomaterial for biomedical applications, offering a unique combination of tunable surface chemistry, high electrical conductivity, mechanical flexibility, and biocompatibility. These superior properties, coupled with its facile and mask-free fabrication process, have positioned LIG as a promising platform for next-generation wearable and point-of-care sensors. This review presents a comprehensive overview of LIG synthesis, microstructures, properties, and functionalization strategies, with a particular focus on its applications in health monitoring and diagnostics. We highlight recent advances in LIG-based sensors for detecting physical, electrophysiological, chemical, and biochemical signals. Key challenges including material variability, miniaturization, scalability, stability, and biocompatibility are critically discussed. Finally, we explore future directions for integrating LIG biomedical sensors with emerging technologies such as artificial intelligence, big data, and eco-friendly materials to enable intelligent, personalized, and sustainable healthcare solutions.

1. Introduction

In recent years, the growing demand for real-time health monitoring has driven the development of biomedical sensors and diagnostic devices. Current conventional clinical diagnostics often rely on well-equipped laboratories, bulky instruments, and trained personnel, making them unsuitable for point-of-care monitoring. In contrast, wearable biomedical sensors offer a promising solution by enabling continuous and non-invasive tracking of physiological signals and biochemical markers directly from the human body, thereby supporting personalized healthcare and promoting early disease detection.

Among various materials used for biomedical sensors, graphene and its derivatives have received considerable attention due to their outstanding properties, including excellent electron mobility (200 000 $cm^2\ V^{-1}\ s^{-1}$),[1] high thermal conductivity (4840–5300 $W\ m^{-1}\ K^{-1}$),[2] mechanical strength (1 TPa),[3] large specific surface area (2630 $m^2\ g^{-1}$),[4] and good biocompatibility. These characteristics make graphene highly suitable for diverse applications, including sensors, high-speed electronics, optoelectronics, and energy storage devices.[5] Conventional methods for producing graphene include mechanical exfoliation, chemical vapor deposition (CVD), liquid-phase exfoliation, and the reduction of graphene oxide.[5] However, these techniques are often complex, time-consuming, and may involve toxic chemicals or solvents, which limit the large-scale production and commercialization of graphene-based biomedical devices.

To overcome these limitations, laser-induced graphene (LIG) has emerged as a promising alternative (Fig. 1). LIG is synthesized by directly irradiating a focused laser beam onto carbon-rich precursors, such as synthetic polymers (*e.g.*, polyimide (PI), polyether ether ketone (PEEK)),[6,7] natural materials (*e.g.*, wood, leaves),[8,9] food-based materials (*e.g.*, bread, sugar),[10,11] and even heavy hydrocarbons.[12] The laser locally converts the material into a porous graphene-like structure through rapid heating at extremely high temperatures.[13,14] This one-step, maskless, and cleanroom-free process enables simultaneous material conversion and direct patterning, significantly enhancing productivity and reducing fabrication costs. The microstructure, crystallinity, and surface chemistry of LIG can be

[a] Department of Biomedical Engineering, National University of Singapore, Singapore 117583, Singapore. E-mail: ctlim@nus.edu.sg
[b] Singapore Institute of Manufacturing Technology (SIMTech), Agency for Science, Technology and Research (A*STAR), Singapore 138634, Singapore
[c] Institute for Health Innovation & Technology (iHealthtech), National University of Singapore, Singapore 117599, Singapore
[d] Mechanobiology Institute, National University of Singapore, Singapore 117411, Singapore
[e] Institute for Functional Intelligent Materials, National University of Singapore, Singapore 117544, Singapore

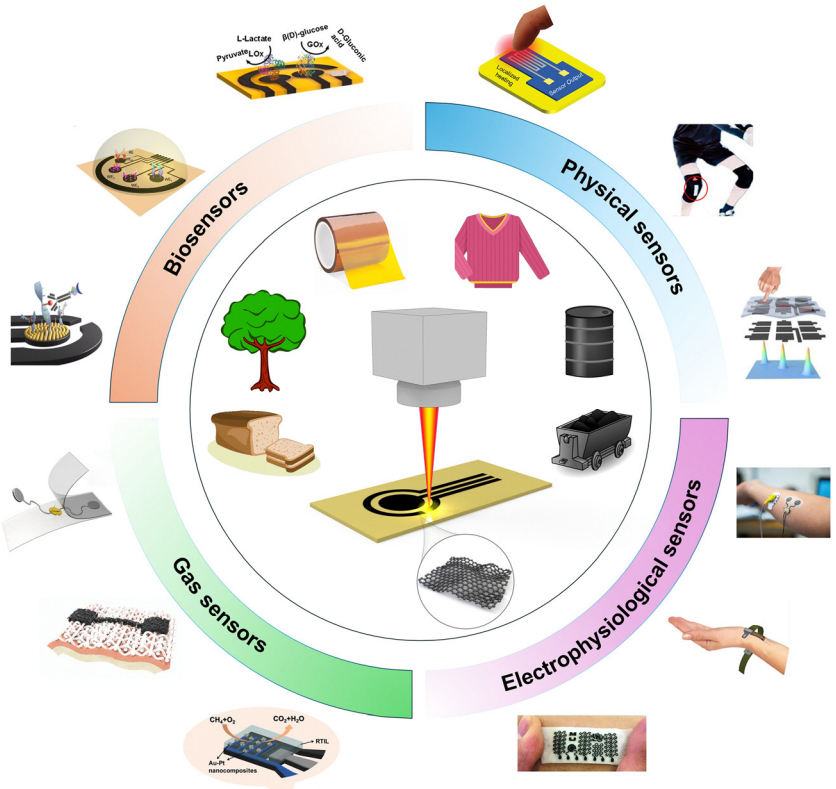

Fig. 1 Schematic illustration of LIG fabrication. Various carbon-rich precursors, including bread, wood, leaves, PI, cotton fabric, heavy hydrocarbons, and coal, can be directly converted into LIG through laser irradiation. The resulting LIG can be applied in a wide range of biomedical applications, including physical, electrophysiological, biosensors, and gas sensors. Reproduced with permission.[16] Copyright 2024, Springer Nature. Reproduced with permission.[17] Copyright 2022, American Chemical Society. Reproduced with permission.[18] Copyright 2024, American Chemical Society. Reproduced with permission.[19] Copyright 2020, American Chemical Society. Reproduced with permission.[20] Copyright 2020, John Wiley & Sons, Inc. Reproduced with permission.[21] Copyright 2018, Wiley-VCH Verlag. Reproduced with permission.[22] Copyright 2024, MDPI. Reproduced with permission.[23] Copyright 2022, American Chemical Society. Reproduced with permission.[24] Copyright 2022, Springer Nature. Reproduced with permission.[25] Copyright 2024, Royal Society of Chemistry. Reproduced with permission.[26] Copyright 2020, Cell Press (Elsevier). Reproduced with permission.[27] Copyright 2025, Elsevier.

precisely tailored by adjusting laser parameters such as power, scanning speed, wavelength, and ambient conditions.[9,15] Compared to other graphene-like materials, LIG exhibits superior electrical conductivity and structural quality, as supported by multiple characterization results reported in the literature.[6,9]

The ability to directly pattern LIG with high resolution makes it well-suited for micro- and nanoscale fabrication. Moreover, the laser processing parameters can be easily adjusted, allowing spatial control over the material's properties and microstructures within a single design. In biomedical applications, LIG is also highly compatible with various functionalization strategies, enabling selective and sensitive detection of diverse stimuli. This versatility allows multiple sensing modalities to be integrated into a single, low-cost, and disposable platform, making it well suited for smart healthcare systems, wearable electronics, and environmental monitoring. Furthermore, the integration of LIG-based sensing platforms with the internet of things, artificial intelligence, and big data technologies is expected to accelerate the advancement of data-driven healthcare and intelligent diagnostic systems.

To fully realize the potential of LIG in biomedical applications, a deep understanding of its formation mechanisms, structures, properties, and the influence of fabrication parameters is essential. Although several reviews have discussed LIG and its applications, there is still a lack of in-depth analyzes specifically focused on its role in biomedical sensors and health monitoring. This review aims to fill that gap by providing a detailed overview of the fundamental aspects of LIG, intended for researchers in the biomedical field as well as those utilizing LIG in related research areas. In particular, we highlight recent advances in LIG-based biomedical sensors, with an emphasis on flexible, wearable, and point-of-care systems designed for health monitoring and medical diagnostics. Through these insights, this review provides a foundation for the development of next-generation LIG-enabled technologies for healthcare applications.

2. Formation mechanism and fabrication of LIG

2.1. Mechanism of LIG formation

A comprehensive understanding of the mechanisms underlying LIG formation is crucial for tailoring its structures and properties for specific applications. Lasers, with their highly coherent, monochromatic, and directional beams, allow for precise and

localized energy delivery, making them excellent tools for controlled material transformation.[28] When a laser beam irradiates a carbon precursor, its optical energy is rapidly absorbed and converted into heat. The tightly focused laser beam results in intense and localized heating within an extremely short time scale. This rapid temperature increase provides the energy needed to break chemical bonds such as C–O, C═O, C–H, and C–N, initiating the transformation process.[6,13] Subsequently, sp^3-hybridized carbon atoms undergo structural rearrangement into sp^2-hybridized carbon atoms, forming graphitic domains (Fig. 2a–d).[6] Chyan *et al.* proposed that amorphous carbon acts as an intermediate state during the transition from carbon precursors to LIG.[10] They also demonstrated that multiple laser irradiations can facilitate LIG fabrication on various substrates, as long as these materials are capable of preliminary carbonization through thermal, photochemical, or chemical processes. Kim *et al.* further detailed the LIG formation mechanism, describing it as a sequence involving carbonization, graphitization, and exfoliation.[29] Carbonization initiates at temperatures between 250–500 °C, releasing heteroatoms (*e.g.*, oxygen and nitrogen) as gaseous byproducts and leaving amorphous carbon. Graphitization begins at significantly higher temperatures, up to approximately 3000 K, where amorphous carbon reorganizes into sp^2-bonded graphitic structures. Exfoliation, the final step, separates graphene layers through thermal expansion or athermal Coulombic forces.[30,31]

Using molecular dynamics (MD) simulations, Chen *et al.* provided deeper insights into LIG formation from PI at high temperatures (Fig. 2e).[14] PI molecules decomposed into smaller fragments when heated from 300 K to 3000 K. Maintaining the temperature at 3000 K (>250 ps) gradually increased the number of carbon rings. After about 600 ps, carbon clusters emerged with numerous defects initially, which later self-repaired during cooling back to room temperature over another 600 ps, forming nearly defect-free graphene networks. This study emphasized the importance of heating duration and temperature, demonstrating that sufficient heating periods are crucial for producing high-quality graphene. Besides, optimizing the spacing between laser pulses maintains the

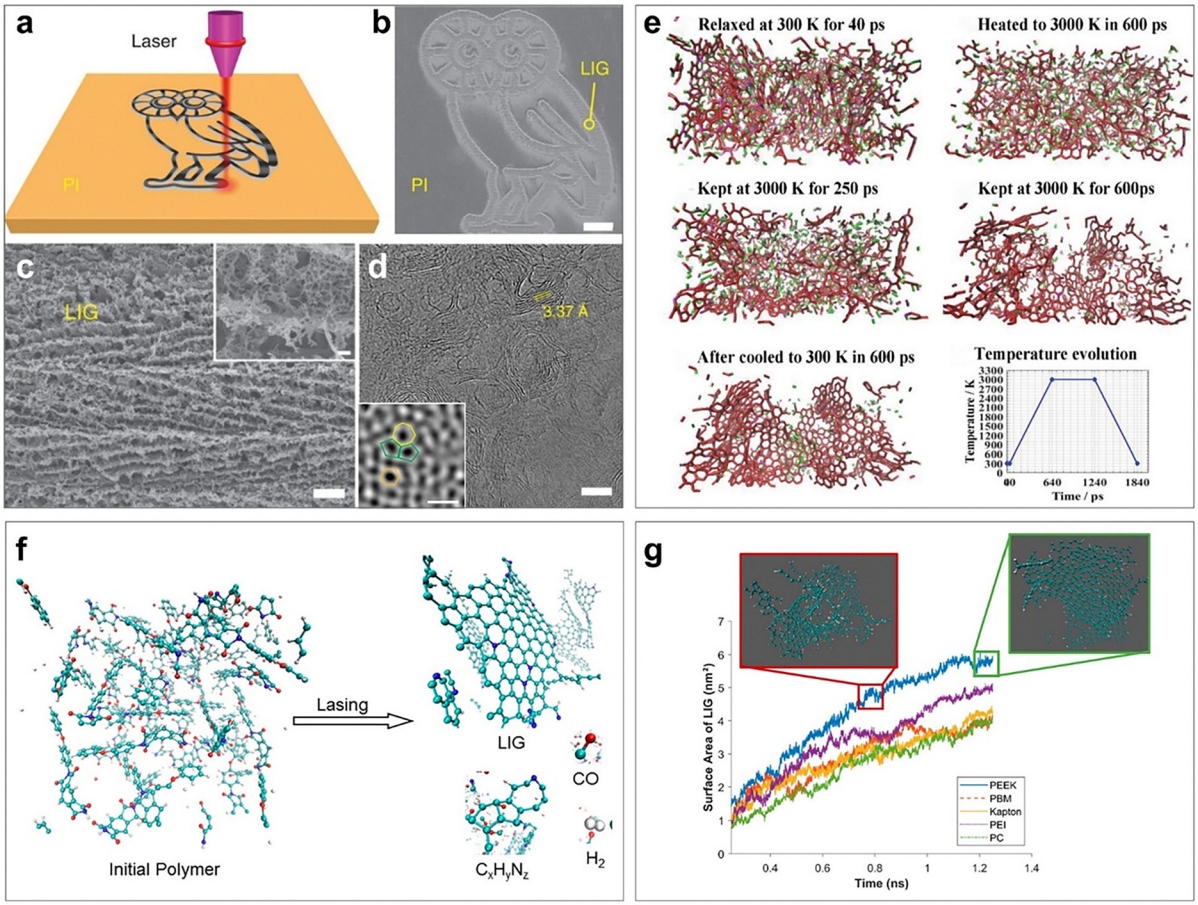

Fig. 2 (a) Schematic illustrating the fabrication of LIG on a PI substrate. (b) SEM image displaying an owl-shaped LIG pattern on PI substrate. Scale bar: 1 mm. (c) Zoomed-in SEM image of LIG. Scale bar: 10 μm. (d) High-resolution TEM image of LIG. Scale bar: 5 nm. Reproduced with permission.[6] Copyright 2014, Springer Nature. (e) Snapshots from MD simulations during the rapid heating and cooling process. Reproduced with permission.[14] Copyright 2019, Wiley-VCH Verlag. (f) Simulation results depicting the transformation of polymers into LIG along with CO, H_2, and hydrocarbon molecules. (g) Changes in the surface area of LIG produced from five different polymers, with temperatures reaching 3000 K between 0.2 and 1.25 ns. Two insets show LIG structures produced from PEEK at 0.8 ns and 1.2 ns. Reproduced with permission.[13] Copyright 2020, American Chemical Society.

required reaction temperature. Sufficiently high temperatures (*i.e.*, 3000 K) were essential, as no graphene structures formed at 2400 K. During the formation of LIG, gases such as H_2O, N_2, H_2, and CO were generated, which helped minimize oxidation and facilitated the growth of larger graphitic clusters.[32] Furthermore, MD simulations showed graphene-like clusters with heptagonal and pentagonal rings, aligning well with previous TEM observations.[6]

Beyond PI, various polymers can also be converted into LIG *via* CO_2 laser irradiation. Vashisth *et al.* explored LIG formation from polybenzimidazole (PBI), PEEK, polyetherimide (PEI), and polycarbonate (PC) using reactive MD simulations (Fig. 2f).[13] Their findings indicated optimal LIG formation temperatures between 2500 and 3000 K. Initially, an amorphous carbon structure formed rapidly (within 0.2 ns), subsequently transforming into ordered graphitic structures containing 5- and 7-membered rings after approximately 0.8–1.2 ns (Fig. 2g). Simulation results showed significantly higher LIG yields under inert atmospheres compared to oxygen-rich environments. Notably, PEEK and PEI yielded LIG with larger surface areas, making them preferable for sensing and energy storage applications. PBI demonstrated the highest yield, attributed to the absence of oxygen in its polymer backbone. Although engineering plastics with high thermal stability are suitable for LIG production, vinyl polymers and thermally less stable materials tend to depolymerize or ablate rather than form graphene structures.[10] Consequently, careful precursor selection is essential for successful LIG production.

In addition to synthetic polymers, lignocellulosic materials have also been investigated for LIG fabrication. Ye *et al.* employed CO_2 lasers to induce LIG formation from wood under inert atmosphere.[15] Their findings revealed that wood, which is primarily composed of lignin, cellulose, and hemicellulose, exhibits relatively low thermal stability. As a result, laser irradiation under ambient conditions led to severe ablation rather than LIG formation. This study highlighted lignin's critical role in successful graphitization, which is due to its high aromatic carbon content and thermal stability. In a subsequent study, they applied multiple lasing and defocusing techniques to successfully produce LIG from lignocellulosic materials under ambient conditions.[10] This was achieved using substrates with high lignin content, such as cork, coconut shell, and potato skins, which contain approximately 25%, 30%, and 36% lignin, respectively. In addition, they demonstrated that phosphate-based flame retardants can enhance the thermal stability of carbon precursors, thereby enabling LIG formation on highly flammable substrates such as paper and textiles.

Since lasers serve as the energy source for converting carbon precursors into LIG, the choice of laser type significantly affects LIG formation. While CO_2 lasers (wavelength of 10.6 μm, continuous wave to microsecond pulses) are commonly used, Le *et al.* introduced ultraviolet (UV) femtosecond lasers to directly convert natural wood and dried leaves into LIG under ambient conditions, eliminating requirements for controlled atmospheres, multiple lasing strategy, or flame-retardant treatments.[8,29] They proposed that ultrashort laser pulses generate stable temperatures between 348–634 °C which convert wood into thermally stable amorphous carbon and preventing ablation. Moreover, the extremely high energy delivered by ultrashort pulses enables rapid sp^3-to-sp^2 carbon transformation *via* thermal and nonthermal phase transitions.[33] Nonthermal transitions occur directly under high electron–hole plasma densities, whereas lower densities trigger thermal transitions at temperatures lower than those in conventional methods.[34] As a result, ultrashort pulsed lasers improve conversion efficiency and significantly reduce thermal ablation compared to conventional long-pulsed lasers.[8,29]

2.2. Fabrication and modification of LIG

2.2.1. Laser sources. Lasers are the primary tools used to convert carbon precursors into LIG. Therefore, selecting an appropriate laser source critically impacts successful LIG formation, as well as the microstructure and properties of the resulting material. Various lasers have been employed for LIG fabrication, covering wavelengths from UV to mid-infrared (MIR) (Fig. 3a and b).[6,35,36] Among these, CO_2 lasers are most commonly used due to their affordability, low operational cost, robustness, and strong absorption by polymers and organic substances.[28] Typically, CO_2 lasers operate at wavelengths of 9.3–10.6 μm, with pulse durations ranging from continuous wave (CW) to microseconds. However, CO_2 lasers inherently provide low spatial resolution due to their long wavelengths. According to the Abbe diffraction limit, spatial resolution is inversely proportional to the wavelength; thus, shorter wavelengths yield higher resolution.[37,38] Generally, CO_2-laser-produced LIG features exhibit minimum linewidths of around 60–120 μm,[28,39] relatively large compared to shorter wavelength lasers. For example, Stanford *et al.* achieved 12 μm spatial resolution using a 405 nm laser.[36] This limitation restricts the use of CO_2 lasers in applications that require micrometer-scale precision.

UV (100–400 nm) lasers have also gained considerable attention for LIG fabrication, owing to their shorter wavelengths and higher photon energies, which allow precise photothermal and photochemical interactions with carbon precursors.[35,40] Notable examples of UV lasers include excimer lasers such as ArF (193 nm), KrF (248 nm), and XeCl (308 nm), which are known for delivering high-energy pulses suitable for precise microfabrication and patterning.[28] Additionally, UV diode lasers in the 375–405 nm range have emerged as attractive options due to their affordability, compact size, and compatibility with compact fabrication setups.[41] UV wavelengths are strongly absorbed by carbon precursors, enhancing overall conversion efficiency and enabling LIG feature resolutions as fine as 10–15 μm, depending on optical configurations and material properties.[36]

Visible-wavelength (400–750 nm) lasers have also been explored;[42–44] however, material absorption at these wavelengths varies significantly and is generally lower than absorption in the UV region. Xing *et al.* showed that PI absorbs significantly less in the visible range than in the UV range.[45] Similarly, Le *et al.* analyzed the UV-vis-NIR absorption spectrum

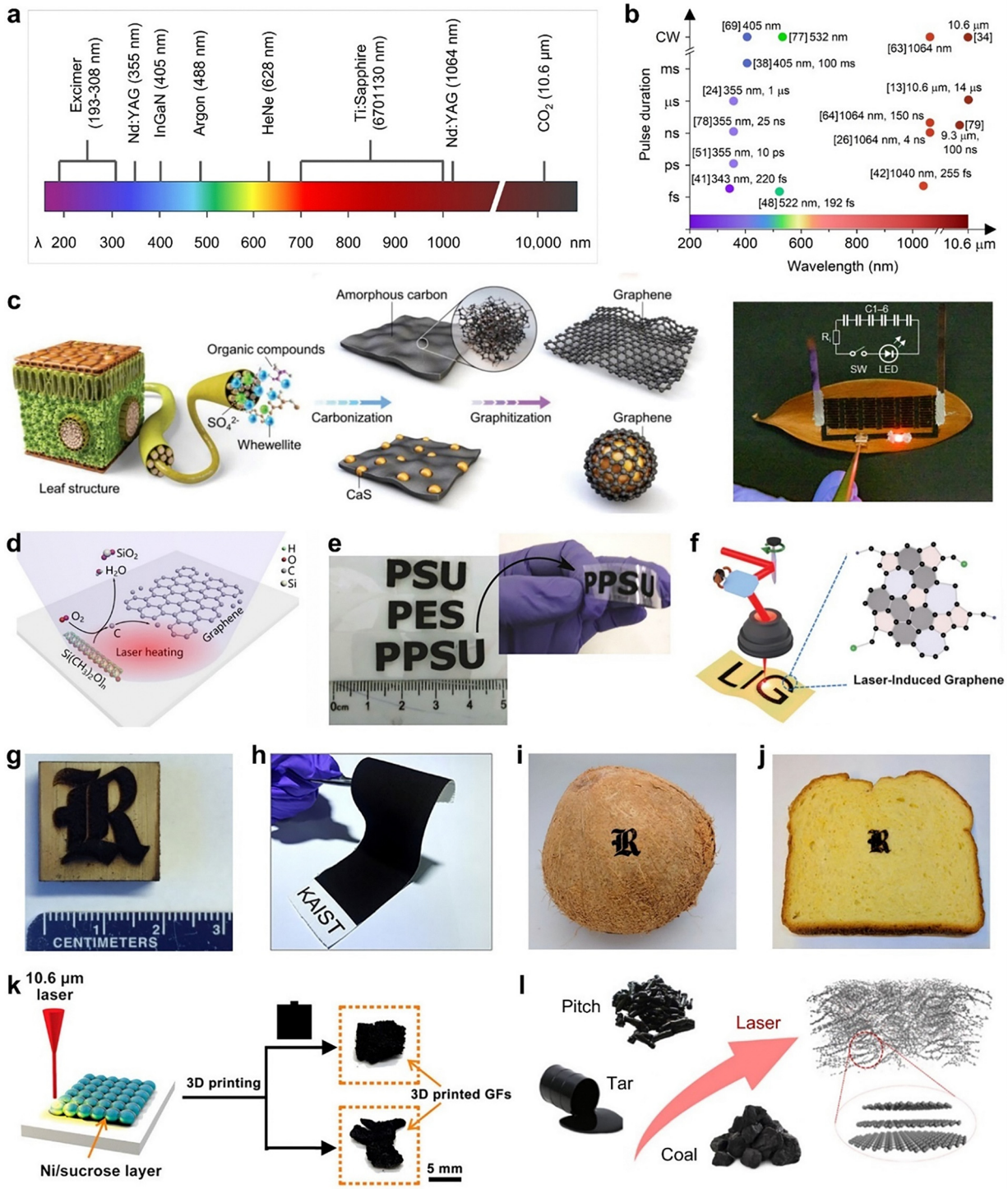

Fig. 3 (a) Most commonly used laser types across the optical spectrum. (b) Lasers used for LIG fabrication, categorized by wavelength and pulse duration. Reproduced with permission.[69] Copyright 2022, Wiley-VCH Verlag. (c) Left: Schematic illustration showing the conversion of dried leaf into LIG under laser irradiation. Right: LIG MSCs on a leaf powering a red LED. Reproduced with permission.[8] Copyright 2022, Wiley-VCH Verlag. (d) Conversion of PDMS into LIG. Reproduced with permission.[56] Copyright 2019, American Chemical Society. LIG patterns on (e) PSU, PES, and PPSU polymers, (f) Kevlar textile, (g) wood, (h) cotton fabric, (i) coconut shell, (j) bread. (k) Schematic illustration of *in situ* 3D graphene foam synthesis. (l) Laser-induced conversion of heavy hydrocarbons (*e.g.*, pitch, tar, coal) into LIG. Reproduced with permission.[57] Copyright 2018, American Chemical Society. Reproduced with permission.[70] Copyright 2025, Wiley-VCH Verlag. Reproduced with permission.[15] Copyright 2017, Wiley-VCH Verlag. Reproduced with permission.[47] Copyright 2024, American Chemical Society. Reproduced with permission.[10] Copyright 2018, American Chemical Society. Reproduced with permission.[11] Copyright 2017, American Chemical Society. Reproduced with permission.[12] Copyright 2020, American Association for the Advancement of Science.

of dried leaves, reporting absorption of 95% at 346 nm, which decreased to 92% at 520 nm and further dropped to 61% at 700 nm.[8] Therefore, careful consideration of material optical properties is necessary for effective LIG fabrication using visible-wavelength lasers.

Near-infrared (NIR) lasers, typically operating within the 800–1064 nm range, have been widely utilized in industrial applications such as material cutting and welding. Yb:YAG and Nd:YAG lasers represent typical examples.[28] Although a few research groups have demonstrated LIG fabrication with NIR lasers,[46] their overall use in LIG research remains limited. This is likely due to the low absorption of NIR wavelengths by most carbon precursors. Le *et al.* reported that dried leaves and cotton fabric absorbed only about 37% and 21% of incident 1064 nm radiation, respectively, which is significantly lower than their absorption at UV wavelengths.[8,47]

Lasers are also classified by pulse duration, ranging from CW to ultrashort femtosecond pulses (1 fs = 10^{-15} s). Numerous studies have successfully demonstrated LIG formation using lasers with pulse durations from CW to picoseconds (ps), where the photothermal effect primarily drives the conversion mechanism.[6,14,29,36,48,49] Notably, shortening pulse durations to the femtosecond regime induces unique phenomena. Femtosecond lasers, characterized by ultrashort pulse widths and extremely high peak intensities, produce minimal heat-affected zones and promote more efficient multiphoton absorption processes.[50,51] In addition, femtosecond lasers can facilitate the nonthermal or low-temperature conversion of sp^3 to sp^2 carbon atoms.[34] Taking these advantages, Kim's group fabricated LIG microsupercapacitors (MSCs) directly onto thin leaves using a UV femtosecond laser (346 nm, 255 fs) (Fig. 3c).[8] Similarly, Morosawa *et al.* successfully used a green femtosecond laser (522 nm, 192 fs) to produce LIG on transparent cellulose nanofiber films under ambient conditions. They highlighted multiphoton absorption as a key contributor, due to the weak absorption of green light by the cellulose nanofibers.[52] Despite these advantages, femtosecond lasers are generally more expensive, although their prices have decreased significantly due to technological advancements and wider commercial adoption.

In summary, lasers with strong absorption by carbon precursors are suitable for LIG fabrication. Selecting lasers with optimized absorption wavelengths improves conversion efficiency and energy utilization. For instance, Tour's group observed that LIG formation on PI required 2.3 times lower laser fluence, defined as the energy delivered per unit area, when employing a 9.3 μm CO_2 laser (2.1 J cm^{-2}) compared to a 10.6 μm CO_2 laser (4.9 J cm^{-2}).[39] Furthermore, shorter laser wavelengths inherently provide higher spatial resolution, since the optical diffraction limit in laser processing defines the smallest achievable feature size as being directly related to the wavelength of the laser beam.

2.2.2. Fabrication parameters. Based on the mechanism described above, it is evident that LIG formation primarily relies on the high temperatures generated by laser-material interactions. By carefully controlling fabrication parameters, we can influence the formation, microstructure, and properties of the resulting LIG. Common fabrication parameters include laser power, fluence, scanning speed, repetition rate, and defocusing level.

To investigate the effect of laser power on LIG formation on PI, Lin *et al.* gradually increased laser power from 2.4 W to 5.4 W.[6] They observed that at 2.4 W, the atomic percentage of carbon significantly increased from 71% to 97%, while nitrogen and oxygen content decreased dramatically to below 3%. Thus, 2.4 W was identified as the power threshold for LIG formation. Sheet resistance quantifies the electrical resistance of thin conductive films per unit area and serves as a key metric for evaluating performance in planar electronic devices. At this power level, the LIG exhibited a sheet resistance of 35 Ω sq^{-1}, which is notable considering that PI is an insulating material. Further increasing the laser power to 5.4 W gradually decreased the sheet resistance, achieving the lowest value of 15 Ω sq^{-1} at 5.4 W. However, higher laser powers also increased oxidation, which compromised the LIG's quality due to excessive thermal effects. Apart from laser power, pulsed lasers are often characterized by laser fluence. Duy *et al.* reported a critical laser fluence threshold of 5 J cm^{-2} required to initiate carbonization of PI using a CO_2 laser.[39] Below this threshold (*e.g.*, at 3.5 J cm^{-2}), the structures formed remained as thin sheets of unconverted PI.

In studies on LIG formation on wood, Kim *et al.* obtained similar results.[29] They reported that LIG produced at a laser power of 0.2 W had a sheet resistance of around 100 Ω sq^{-1}, while increasing the power to 0.8 W reduced the resistance to 10 Ω sq^{-1}. Scanning speed also had a significant impact on LIG conductivity, with the lowest sheet resistance achieved at a speed of 10 mm s^{-1}. Both slower and faster speeds resulted in higher sheet resistances. Slower speeds resulted in excessive heating and the formation of microcracks, while faster speeds provided insufficient heat, hindering graphitization and yielding thinner LIG films.

During pulsed laser irradiation, each pulse deposits a specific amount of heat onto the carbon precursors. The accumulation of heat from multiple pulses builds a stable temperature base for carbonization. Therefore, the repetition rate of pulsed lasers is a crucial parameter.[9,53] Kim's group demonstrated that LIG could not form on wood at repetition rates below 100 kHz when using a UV femtosecond laser (343 nm, 220 fs).[29] Moreover, increasing repetition rates from 100 kHz to 500 kHz notably enhanced LIG quality.

Defocusing level, referring to the displacement between the laser focal point and the substrate surface, is another important parameter. PEI typically yields lower-quality LIG compared to PI.[6,10] However, Chyan *et al.* successfully generated LIG on PEI by defocusing the laser beam by 0.75 mm, achieving sheet resistances comparable to those of PI (~15 Ω sq^{-1}).[10] Lowering the substrate by 1 mm increased the laser spot size from 175 μm to 300 μm, effectively tripling the exposure area while maintaining the same dot density. This reduced thermal ablation and improved LIG yield, although it resulted in lower patterning resolution due to the larger spot size.

All the fabrication parameters discussed above aim to manage the photothermal effect within an optimal range for efficient LIG formation. Insufficient photothermal energy hinders LIG formation, while excessive energy can degrade LIG quality due to thermal damage and oxidation. Other parameters such as pulse stacking density (pulses per inch, PPI), printing resolution (dots per inch, DPI), scanning strategy, and hatch spacing also play crucial roles. This section highlights important and popular parameters for reference, but other parameters not included here also play a role in controlling the photothermal effect during LIG fabrication.

2.2.3. Carbon precursors. PI was the first material employed for LIG fabrication.[6] Since then, various carbon precursors have demonstrated the capability to produce LIG under appropriate fabrication parameters, pre-treatment processes, and environmental conditions. These carbon precursors can be classified into three main categories. The first category includes synthetic polymers, which are engineered materials with well-defined and uniform structures. Examples include PEEK,[7] polytetrafluoroethylene (Teflon),[54] Kevlar (*para*-aramid),[55] polydimethylsiloxane (PDMS),[56] polysulfone (PSU), poly(ether sulfone) (PES), polyphenylsulfone (PPSU),[57] and phenolic resin (Fig. 3d–f).[58] Due to their consistent chemical composition, high thermal stability, and robust mechanical properties, synthetic polymers typically produce LIG with excellent electrical conductivity. For example, Yang *et al.* successfully fabricated LIG on Kevlar textiles, achieving a sheet resistance as low as 2.86 Ω sq^{-1}.[55] A significant advantage of synthetic polymers is their high uniformity, low impurity levels, and stable chemical composition, which facilitate the production of LIG with consistent structures and properties. However, the environmental impact of synthetic polymers must be carefully considered, as their poor biodegradability contributes to electronic waste and raises sustainability concerns.

The second category comprises natural biomass-derived precursors, including lignocellulosic and food-based materials. Lignocellulosic materials, such as wood, dried leaves, cork, coconut shell, cotton fabric, and paper, are rich in cellulose, hemicellulose, and lignin (Fig. 3g–i).[8,10,29,47] These precursors are naturally sourced, highly abundant, widely available, inexpensive, and eco-friendly. However, their chemical composition is generally less uniform and consistent than that of synthetic polymers, leading to variations in the properties of the resulting LIG. Due to higher aromatic carbon content and superior thermal stability, lignin-rich materials generally produce LIG with greater degree of graphitization.[15] To enhance the thermal stability of materials with high cellulose or hemicellulose content, some researchers have utilized flame-retardants.[10] LIG produced from precursors in this category also demonstrates relatively good electrical conductivity. For instance, LIG on wood could achieve an excellent sheet resistance of 10 Ω sq^{-1}.[29] Another subcategory includes food-based materials containing carbohydrates that can be carbonized, such as bread and sucrose (Fig. 3j and k). Due to their poor thermal stability, these materials require pre-treatment prior to LIG fabrication. For instance, Chyan *et al.* used a 1-mm defocused CO_2 laser beam to convert the surface of bread into char (amorphous carbon) before applying a second laser scan to transform the char into LIG.[10] Similarly, Sha *et al.* mixed sucrose with nickel to facilitate its conversion into LIG (Fig. 3k), as nickel is known to promote graphene growth in CVD processes.[11,59]

The third group comprises hydrocarbon-rich materials, such as coal, tar, and pitch (Fig. 3l). These materials vary widely in their H : C ratio, aromatic content, and initial structural alignment. By adjusting the laser power, speed, and focus of a CO_2 laser, the H : C ratio, sp^2 content, and graphitization level of LIG could be precisely controlled.[12] The resulting LIG films could achieve an excellent electrical conductivity of up to 1000 S m^{-1}.

2.2.4. Environmental effects. The formation of LIG occurs when carbon precursors are heated to several thousand degrees celsius, making the fabrication environment a significant influencing factor. For instance, Ye *et al.* studied LIG formation on wood and found that direct irradiation with a CO_2 laser in ambient air caused severe material ablation without producing LIG.[15] This was attributed to the reaction between wood and oxygen, resulting in decomposition of the lignocellulosic structure. When they conducted LIG fabrication in a nitrogen atmosphere, they successfully produced LIG on wood with an excellent sheet resistance of 10 Ω sq^{-1}. Similarly, other studies have demonstrated that fabricating LIG in inert gas atmospheres reduces thermal damage and oxidation, increases carbon yield, and produces in higher-quality LIG.[60]

The fabrication atmosphere also influences the surface properties of LIG. Li *et al.* fabricated LIG on PI using a CO_2 laser under various atmospheres, including ambient air, O_2, H_2, and Ar.[61] They found that LIG prepared in ambient air and O_2 was hydrophilic, exhibiting a water contact angle of around 0°. In contrast, LIG produced in Ar or H_2 atmospheres showed significantly increased hydrophobicity, with water contact angles of about 150°. Moreover, samples with lower oxygen content and fewer C–O bonds consistently demonstrated higher water contact angles. When fabricated in ambient air or O_2, LIG undergoes oxidation at high temperatures, leading to increased O and C–O bond content, whereas no such oxidation occurred in inert atmospheres (Ar or H_2). Furthermore, the fabrication environment can incorporate doping elements into LIG structures. For instance, conducting the fabrication in an SF_6 atmosphere results in fluorine-doped LIG (F-doped LIG). The formation of C–F bonds and reduced surface energy enhance the hydrophobicity of LIG, achieving water contact angles exceeding 160°.

2.2.5. Transfer techniques. After being fabricated on a carbon precursor, LIG can either be used directly or transferred onto another substrate with desirable properties for specific applications. Besides, due to its relatively low mechanical robustness, LIG is susceptible to damage from external impact. Therefore, forming LIG–polymer composites can significantly enhance its mechanical durability. Common transfer techniques include polymer-assisted transfer, mechanical transfer, and thermal-assisted transfer.

Polymer-assisted transfer of LIG is a widely adopted technique due to its simplicity, efficiency, and versatility. This method

leverages the highly porous structure of LIG, which enables a liquid polymer precursor to infiltrate and establish a percolation network. After LIG is produced on a substrate, a liquid polymer precursor is poured onto it and subsequently cured to form a solid and mechanically stable layer. When the polymer is peeled from the carbon precursor, the LIG is transferred with it, forming a robust LIG–polymer composite. Commonly used polymers for this technique include PDMS,[62,63] Ecoflex,[64] polyurethane (PU),[19] and polyvinyl alcohol (PVA).[65] The resulting LIG composites exhibit excellent stretchability, ranging from 50% to 100%, depending on the polymer's properties and the substrate's dimensions. However, when the polymer layer thickness is reduced to <45 μm, transfer becomes difficult due to insufficient interfacial adhesion.[16] To address this, Lu *et al.* developed a cryogenic LIG transfer method, enabling the transfer of LIG from PI to an ultrathin (1.0–1.5 μm) adhesive hydrogel composed of PVA–phytic acid (PA)–honey (PPH).[16] Due to its ultrathin nature, the LIG-PPH composite exhibits stretchability ranging from 20% to 110%, with up to 220% possible through structural optimization.

Mechanical transfer is a straightforward technique for transferring LIG from a carbon substrate to another substrate. The porous structure of LIG results in relatively weak interaction to the carbon substrate, allowing for easy detachment. Therefore, LIG on PI can be effectively transferred by using adhesive tapes. For instance, Pinheiro *et al.* synthesized LIG on fire-retardant-treated paper using a CO_2 laser and successfully transferred LIG electrodes to stretchable PU medical tape.[66] These electrodes functioned as strain sensors, accommodating up to 10% strain and maintaining stability over 3600 cycles. Similarly, Xu *et al.* transferred LIG from a PI film to medical PU tape, forming an electrode array to capture signals for eye movement and tactile perception.[67] Nevertheless, transferring LIG using adhesive tape does not provide the same level of mechanical robustness and stability as LIG–polymer composites.

Hot pressing is another effective method for transferring LIG. Filler materials are applied to LIG on a PI substrate and then subjected to high pressure and temperature, allowing the fillers to infiltrate the porous structure of the as-produced LIG.[68] The resulting solidified composite is flipped upside down, and the PI substrate is peeled away to reveal the LIG-composite surface. LIG can be combined with diverse filler materials, including latex paint, Portland cement, alkaline-activated geopolymer, and commercial plastics such as polyethylene (PE), polypropylene (PP), and polystyrene (PS). This technique is simple, rapid, and well-suited for commercialization *via* roll-to-roll processing.

3. Microstructures and properties of LIG

3.1. Microstructures

LIG is known for its highly porous structure with large specific surface area ($\sim$340 m^2 g^{-1}),[6] making it ideal for sensing and energy storage. LIG microstructures exhibit considerable variation, primarily influenced by fabrication parameters and carbon precursors. Beyond the sheet-like structures synthesized on PI, as illustrated in Fig. 2c, additional morphologies have also been reported. Duy *et al.* demonstrated that at laser fluences exceeding 40 J cm^{-2}, LIG structures undergo significant morphological changes from sheet-like forms into vertically aligned fibers reaching heights up to 1 mm (Fig. 4a and b).[39] Notably, MSCs based on these fiber-like LIG structures exhibited twice the specific areal capacitance compared to conventional sheet-like LIG structures. Hong *et al.* also explored how other fabrication parameters influence LIG morphology.[40] During laser scanning, the laser beam size varies owing to the tilted PI substrate, resulting in continuous changes in laser fluence. Combining with adjusting scan rate and hatch spacing, five distinct LIG microstructures could be achieved.

Under certain conditions, Kim *et al.* observed that LIG could detach from the PI substrate, forming freestanding helical structures (Fig. 4c and d).[43] This "pyrolytic jetting" phenomenon occurs when the PI film is sufficiently thin ($\sim$75 μm) and conformally adheres to a nonpermeable substrate *via* capillary forces. The Gaussian intensity profile of the laser generates a thermal gradient, causing a pressure-induced rupture at the center and initiating exfoliation. Coupled with internal pressure and laser scanning, this leads to the simultaneous formation of right-handed and left-handed helical jets unless intentionally induced asymmetry is introduced. The resultant structures exhibit complex morphologies at macro-, micro-, and nanoscale (Fig. 4e).

Other synthetic polymers such as PEI,[10] PES, and PPSU[57] can also produce porous LIG structures similar to those from PI.[6] These porous LIG structures result from rapid gas generation during fabrication, causing expansion of carbonized materials. In addition, the sublimation of thermally unstable species also contributes to the high porosity.

Unlike synthetic polymers, which typically produce expanded LIG structures, lignocellulosic materials (*e.g.*, wood, leaves, cork) often result in sunken morphologies, as shown in Fig. 4f–i. Le *et al.* observed depressions of 118 μm and 8 μm for LIG derived from wood and leaves, respectively.[8,29] The high aliphatic content (67–74%) in these materials decomposes at relatively low temperatures,[15] causing carbon loss and structural shrinkage. Furthermore, the rigid crystalline cellulose network reinforced by lignin and hydrogen bonds[71] prevents expansion, unlike synthetic polymers with flexible and loosely bonded polymeric chains.

3.2. Surface wettability

Surface wettability is crucial for diverse applications including sensing, electronics, drug delivery, anti-icing, microfluidics, and oil–water separation. Hydrophilic materials promote water spreading through hydrogen bonding, whereas hydrophobic materials repel water. Notably, the surface wettability of LIG can be easily tuned by controlling fabrication parameters and/or the fabrication environment. Li *et al.* demonstrated early tuning of LIG wettability by altering the fabrication atmosphere (Fig. 5a–c).[61] LIG produced in air or oxygen exhibited

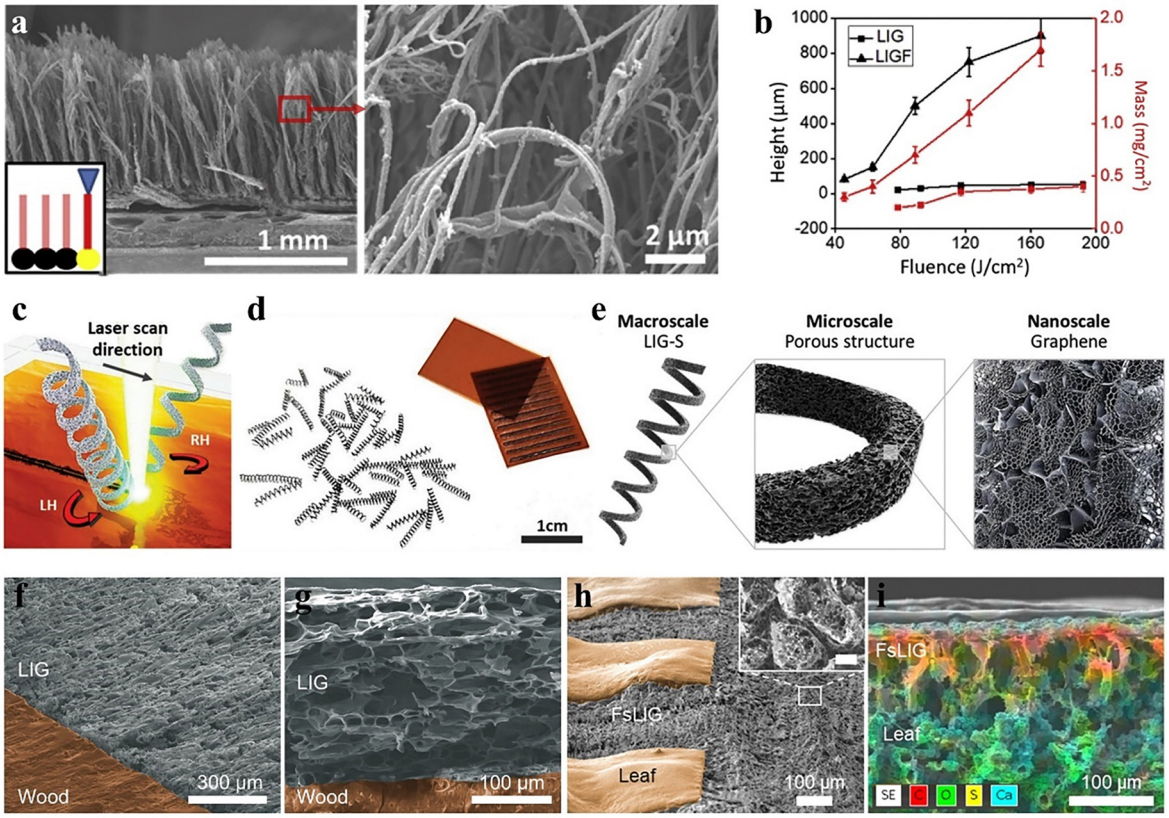

Fig. 4 (a) SEM images of LIG fibers fabricated at a laser fluence of 166 J cm^{-2} and an image density of 500 PPI. (b) Variation in height and mass of LIG and LIG fibers with respect to laser fluence. Reproduced with permission.[39] Copyright 2018, Elsevier. (c) Generation of left-handed (LH) and right-handed (RH) helical LIG-S structures *via* laser scanning. (d) Photographs of multiple LIG-S structures produced from a single PI film. (e) Schematic representation of the resulting LIG-S, highlighting features at the macro-, micro-, and nanoscale levels. Reproduced with permission.[43] Copyright 2023, Wiley-VCH Verlag. (f) Tilted-view and (g) cross-sectional SEM images of LIG formed on wood. Reproduced with permission.[9] Copyright 2019, Wiley-VCH Verlag. (h) Tilted-view and (i) cross-sectional SEM images of LIG on a leaf with corresponding EDS elemental mapping. Reproduced with permission.[8] Copyright 2022, Wiley-VCH Verlag.

superhydrophilicity with water contact angle ≈0° (Fig. 5b and c), while argon or hydrogen atmospheres resulted in superhydrophobic surfaces with contact angle >150° (Fig. 5b and c). Characterization results confirmed that these differences in wetting behavior are attributed to the surface morphology and the surface chemistry of the LIG structures. In particular, fabrication in an SF_6 atmosphere achieved even greater hydrophobicity with contact angle >160° due to the low surface free energy of C–F bonds. The resulting superhydrophobic LIG was successfully applied in oil/water separation and anti-icing applications.

To enable continuous tuning of surface wettability, Wang *et al.* developed a method based on the simultaneous control of surface roughness (6.08–58.18 μm) and fluorine content (0–25.9%).[72] Surface roughness was adjusted by varying the defocusing level (DL) from 0 to 2 mm (Fig. 5d), while fluorine content was modified by dip-coating the LIG in a trimethoxy(1*H*,1*H*,2*H*,2*H*-heptadecafluorodecyl) silane (HFTPS)/isopropanol (IPA) solution with concentrations ranging from 0.4% to 1.6% (Fig. 5e). This method allowed continuously control of LIG wettability from superhydrophilic (contact angle ≈ 0°) to superhydrophobic (contact angle > 150°) for various liquids. Moreover, LIG surfaces could also be tailored to exhibit amphiphilic (DL = 2.0 mm, HFTPS/IPA = 0%), amphiphobic (DL = 0 mm, HFTPS/IPA = 1.6%), and hydrophobic–oleophilic properties (DL = 0 mm, HFTPS/IPA = 0%) (Fig. 5f).

Although effective, many of the aforementioned strategies for tuning LIG wettability involve complex environments or chemical modifications to alter surface chemistry. Another straightforward approach to tuning LIG wettability involves controlling the laser pulse density.[73] By reducing the pulse density from 1000 DPI to 100 DPI, the surface wettability of LIG could be modulated from superhydrophilicity (0°) to superhydrophobicity (>150°) (Fig. 5g). It was observed that a high pulse density promotes surface oxidation and the formation of sheet-like structures, leading to superhydrophilic behavior. In contrast, a low pulse density generates pillar- and hemisphere-like microstructures, with increased surface roughness and reduced oxygen content, leading to superhydrophobic surfaces (contact angle >150°). A significant advantage of this method is the ability to achieve spatial control of surface wettability. For example, liquid patterns and channels were successfully fabricated using superhydrophilic fills and superhydrophobic barriers (Fig. 5h).

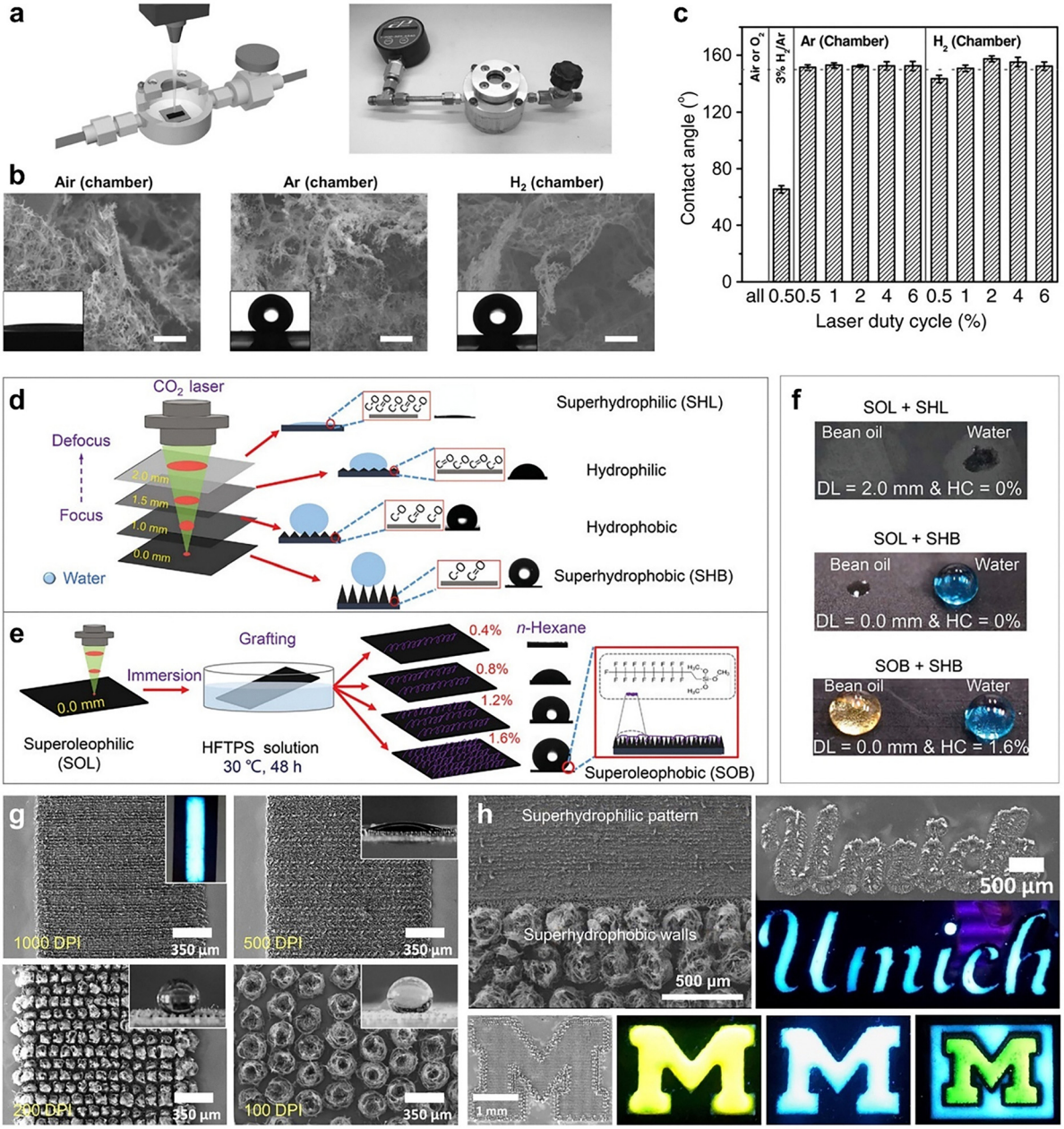

Fig. 5 (a) Left: Schematic illustration of the LIG fabrication process within a controlled atmosphere chamber. Right: Photograph of the actual chamber setup. (b) LIG microstructures formed on PI under different atmospheric conditions (air, Ar, and H_2). Insets show water droplets on the corresponding LIG surfaces. (c) Water contact angles of LIG fabricated under various gas atmospheres. Reproduced with permission.[61] Copyright 2017, Wiley-VCH Verlag. (d) Fabrication of LIG with continuously tunable water wettability by adjusting the laser defocusing level. (e) Modulation of LIG wettability for oil through HFTPS surface functionalization. (f) Demonstration of LIG surfaces exhibiting three distinct wetting behaviors toward water and bean oil. SHL: superhydrophilicity, SHB: superhydrophobicity, SOL: superoleophilicity, SOB: superoleophobicity. Reproduced with permission.[72] Copyright 2021, Wiley-VCH Verlag. (g) Surface morphologies of LIG fabricated at various pulse densities (1000, 500, 200, and 100 DPI). Insets display water droplets on LIG produced at 12% laser output power. (h) SEM images and photographs of liquid patterning using superhydrophilic regions as channels and superhydrophobic boundaries as barriers. Quinine-containing water was used to enable fluorescence under UV illumination for visualizing liquid flow. Reproduced with permission.[73] Copyright 2020, Elsevier.

3.3. Electrical properties

Among graphene-like materials, LIG has emerged as a highly promising candidate due to its outstanding electrical conductivity. Moreover, this conductivity can be precisely tuned by controlling fabrication parameters, and enhanced through the formation of hybrids/composites or flash Joule heating. For instance, Lin *et al.* examined the effect of laser power on the sheet resistance of LIG produced on a PI substrate (Fig. 6a).[6] They observed that increasing the laser power from 2.4 W to 5.4 W led to a reduction in sheet resistance from 32 Ω sq^{-1} to

15 Ω sq^{-1}. The decrease in sheet resistance was particularly steep between 2.4 and 4.2 W, attributed to the photothermal effect that significantly enhances the degree of graphitization. However, beyond 4.2 W, excessive heat generation resulted in increased oxidation, diminishing the quality of LIG and moderating the rate of resistance reduction. This conclusion was further confirmed by complementary Raman spectroscopy and X-ray diffraction (XRD) analyses.

In addition to laser power, the writing speed during laser processing also significantly affects the sheet resistance of LIG. Le *et al.*, in a study focusing on LIG formation on dried leaves, demonstrated that higher writing speeds resulted in increased sheet resistance, whereas slower speeds reduced it (Fig. 6b).[8] They similarly reported that higher laser power improves LIG conductivity, corroborating Lin's findings. By simultaneously controlling laser power and writing speed, they were able to tune the sheet resistance over an extensive range, from 23 Ω sq^{-1} (350 mW, 10 mm s^{-1}) to 1494 Ω sq^{-1} (150 mW, 50 mm s^{-1}).

However, optimizing fabrication parameters may not suffice to achieve lower sheet resistances. For example, LIG derived from wood substrates typically exhibits a lower limit of around 10 Ω sq^{-1}.[15,29] To overcome this limitation, Han *et al.* introduced a strategy to hybridize wood-derived LIG with metal nanostructures, including copper (Cu), cobalt (Co), nickel (Ni), iron (Fe), and nickel–iron (NiFe) (Fig. 6c).[74] In their approach, wood substrates were impregnated with metal nitrate solutions and subsequently dried. During laser processing under an argon atmosphere, the metal salts were thermally reduced to metallic nanoparticles, and the wood was carbonized into LIG. This method produced metal-LIG hybrid structures with significantly improved electrical conductivity, achieving a minimal sheet resistance as low as 3.3 Ω sq^{-1}. These metal-LIG hybrids exhibited enhanced

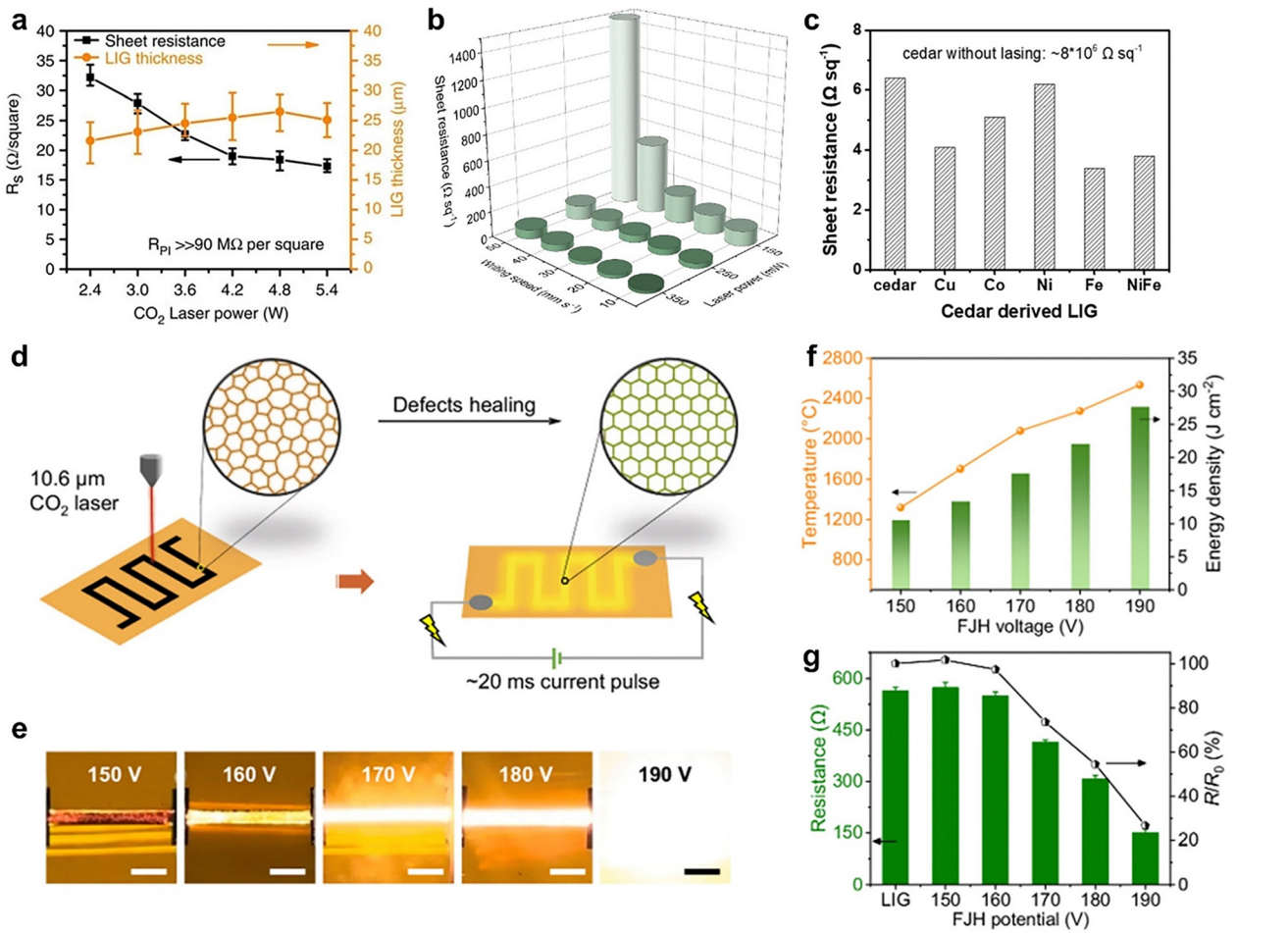

Fig. 6 (a) Correlation between sheet resistance and LIG film thickness as a function of laser power. Reproduced with permission.[6] Copyright 2014, Springer Nature. (b) Sheet resistance of LIG electrodes as a function of laser power and writing speed. Reproduced with permission.[8] Copyright 2022, Wiley-VCH Verlag. (c) Sheet resistance of cedar-derived LIG-metal composites. Reproduced with permission.[74] Copyright 2018, American Chemical Society. (d) Schematic illustration of the F-LIG fabrication process. (e) Photographs of LIG patterns during the flash Joule heating (FJH) process under different applied voltages with a pulse duration of 20 ms. Scale bars: 3 mm. (f) Temperature and areal energy densities achieved during the FJH process. (g) Resistance and resistance reduction ratio (R/R_0) of F-LIG samples compared to original LIG. Reproduced with permission.[75] Copyright 2024, Springer Nature.

performance, making them suitable not only for energy storage and electrocatalysis but also for electromagnetic interference shielding.

Notably, Cheng *et al.* introduced a novel flash Joule heating technique (F-LIG) to further enhance intrinsic LIG conductivity by applying high direct current pulses to pre-patterned LIG (Fig. 6d and e).[75] Under high voltage (150–190 V), LIG undergoes rapid Joule heating, raising local temperatures to between 1300 and 2500 °C (Fig. 6f). These elevated temperatures facilitate graphitization, significantly improving crystallinity, reducing defect density, and increasing crystalline domain size. Consequently, F-LIG exhibited up to a fivefold increase in electrical conductivity compared to untreated LIG (Fig. 6g). Moreover, F-LIG displayed enhanced antibacterial properties under low-voltage conditions, indicating its potential in antimicrobial applications.

3.4. Chemical properties

Graphene is well-known for its exceptional chemical stability, extensively demonstrated through various applications. For instance, graphene has effectively served as a corrosion-resistant coating, enhancing corrosion resistance of metallic substrates like nickel and copper by up to two orders of magnitude in aggressive chloride environments.[76] Moreover, graphene coatings can protect silver substrates from concentrated hydrochloric acid (35–37%) and maintain integrity in heated air up to temperatures of 400 °C.[77] Liu *et al.* studied the chemical durability of pristine graphene membranes immersed in sodium persulfate and sulfuric acid solutions, reporting unchanged conductivity after 15 days.[78] Using X-ray photoelectron spectroscopy (XPS), the absence of characteristic carboxyl group peaks (288.8 eV) indicated no oxidative degradation. Conversely, graphene membranes containing structural defects such as nanopores experience conductivity changes due to gradual oxidation and pore expansion. However, pre-functionalizing nanopores with oxygen-containing groups (OCGs) through oxidation and subsequent chemical reduction with sodium ascorbate effectively stabilizes the membrane conductivity.

During the transformation of carbon precursors into LIG, a significant portion of heteroatoms (*e.g.*, oxygen, nitrogen) is released as gaseous byproducts.[6,29] Remaining heteroatoms integrate into graphene structures as OCGs such as hydroxyl (–OH), carboxyl (–COOH), and carbonyl (–C═O). Consequently, LIG produced in ambient air tends to be hydrophilic due to higher OCG concentrations, whereas LIG fabricated under inert gas atmospheres is hydrophobic due to lower OCG concentrations.[61] This structural arrangement closely resembles graphene frameworks containing nanopores decorated with OCGs, which underpins the remarkable chemical stability of LIG. In fact, LIG has been widely used in robust energy storage devices and electrochemical sensors. Energy storage devices employing LIG electrodes have demonstrated reliable performance across diverse acidic, basic, and saline electrolyte environments.[79]

Furthermore, the presence of OCGs not only impacts the surface properties of LIG but also provides active sites for adsorption and covalent functionalization with various molecules, ranging from small organic compounds to large biomolecules such as enzymes and antibodies.[80,81] By controlling fabrication parameters, the degree of oxidation and graphitization in LIG can be precisely tuned, offering customizable surface chemical reactivity. This combination of chemical robustness and versatile functionalization potential through OCGs has significantly expanded LIG's applicability in diverse sensing applications.

3.5. Biological properties

The toxicity and biocompatibility of nanomaterials are critical concerns, especially when these materials are intended for direct contact with or implantation within biological systems. Certain nanomaterials are known to cause adverse biological effects such as membrane damage, genetic disruption, and apoptosis.[82–84] Therefore, comprehensive evaluations of the biocompatibility and potential toxicity of LIG are essential before its use in biomedical applications. The biological safety of LIG has been extensively studied using zebrafish, chosen due to their significant genetic homology with humans.[85] Experiments involved exposure of zebrafish embryos at various developmental stages to different concentrations of LIG (5, 10, 50, and 100 μg mL^{-1}). Results indicated no negative effects on embryo development or larval behavior, even at the highest tested concentration. This finding notably contrasts with reported toxicities of other graphene-based materials.[82–84] Moreover, the study directly confirmed the biocompatibility of LIG, supporting its safe use in a wide range of biological and biomedical applications.

Based on the biocompatibility and non-toxicity of LIG, Park *et al.* developed flexible and stretchable bioelectronic devices using LIG derived from liquid crystal polymer (LCP) substrates.[86] LCP substrates were chosen specifically due to their superior biocompatibility and minimal moisture absorption (<0.04%) compared to conventional substrates like PI and PDMS. The LIG patterns were designed using kirigami-inspired structures that retained electrical conductivity under biaxial strain of up to 35.7%, enabling conformal contact with biological surfaces. These LIG-based electrodes exhibited reliable performance in on-skin electrophysiological monitoring, including electrocardiogram (ECG) and electromyography (EMG) applications, and were successfully employed as microelectrode arrays for neural interfacing and stimulation. These devices maintained stable operation within physiological ionic environments, further validating LIG's biocompatibility and potential for broader biomedical applications. Wang *et al.* also explored the biological compatibility of LIG by fabricating photothermal Marangoni actuators on PI tape.[87] Biocompatibility was confirmed through cell proliferation assays with MDA-MB-231 cells, demonstrating safe operation within cell culture media. Such results underscore the potential of LIG-based actuators in microfluidic applications.

Beyond biocompatibility, LIG also exhibits intrinsic antimicrobial and self-sterilizing properties.[88,89] Both hydrophilic and hydrophobic variants of LIG demonstrate strong antibacterial activity, with hydrophobic variants displaying slightly higher efficacy (around 7%). The antimicrobial effects of LIG result from physical disruption of bacterial cells through rough surface textures, carbon nanofibers, and porous microstructures, as well as chemical stress induced by surface OCGs (*e.g.*, –COOH, –OH). These interactions compromise bacterial membrane integrity, inhibit adhesion, and induce leakage of cellular contents, ultimately decreasing bacterial viability. As a result, LIG has been effectively integrated into air filtration systems and smart masks[88,89] owing to its antimicrobial capabilities.

Recent studies have also revealed that LIG exhibits promising antiviral properties. Functionalized LIG materials, particularly those with tailored surface potentials or charged states, have demonstrated strong inactivation effects against both enveloped and non-enveloped viruses. For instance, positively charged LIG modified with quaternary pyridinium groups achieved 99–100% inactivation of human coronaviruses HCoV-OC43 and HCoV-229E within 20 minutes under mild conditions, benefiting from synergistic effects between electrostatic interaction and photothermal heating.[90] Separately, capacitance-engineered LIG electrodes charged at low voltages (1–2 V) were shown to exert broad-spectrum antimicrobial action, including significant antiviral activity, without the need for continuous external power or electrolyte solutions.[91] These findings suggest that LIG's antiviral mechanism may involve a combination of electrostatic disruption, electroporation, and oxidative stress, similar to its antibacterial action. Supporting this antiviral potential, previous work has also demonstrated that graphene oxide nanoflakes are effective against Herpes simplex virus type-1 (HSV-1), likely through interactions with the viral envelope that inhibit entry into host cells.[92] Such results further highlight the relevance of graphene-based materials as multifunctional agents for infection control. The ability to tune these effects *via* surface chemistry or electrical charging enhances the versatility of LIG as a promising material for personal protective equipment, air and water purification, and biomedical devices.

In addition, recent studies have begun to investigate the immunomodulatory effects of LIG. *In vivo* experiments involving LIG-based implants have reported minimal immune rejection and inflammatory responses, further supporting its biocompatibility and potential safety in biomedical applications.[93] These findings highlight the importance of assessing immune interactions in parallel with general biocompatibility, as immune modulation plays a critical role in long-term material integration. Similar immunological evaluations have been conducted for other emerging two-dimensional nanomaterials, such as antimonene, where surface functionalization significantly influenced cytokine release in THP-1 cells and enzymatic biodegradation by peroxidases.[94] Therefore, further research is essential to fully elucidate the immunological profile of LIG, particularly under conditions of chronic exposure or implantation.

4. Applications of LIG in health monitoring and diagnostics

4.1. Physical and electrophysiological sensors

4.1.1. Temperature sensors. As homeothermic organisms, humans maintain a stable internal temperature, making body temperature a critical indicator of physiological health. Deviations from normal body temperature, such as hyperthermia or hypothermia, can significantly disrupt metabolic processes, potentially leading to cellular damage, tissue dysfunction, organ failure, or even death in severe cases.[95] Therefore, precise and continuous monitoring of body temperature is crucial for effective health management. Among temperature sensing materials, graphene has been extensively studied due to its outstanding electrical and thermal properties.[5] Notably, graphene exhibits a negative temperature coefficient (NTC), where its electrical resistance decreases with increasing temperature.[96] Furthermore, graphene's high intrinsic thermal conductivity and large surface area facilitate efficient thermal transfer between the stimulus and the sensor, thereby enhancing both sensitivity and response speed.

LIG retains the exceptional properties of graphene while offering practical advantages such as scalable production, low manufacturing costs, and a chemical-free process. The porous microstructure of LIG allows sensors to remain functional under mechanical deformation, providing flexibility and softness superior to conventional metal-based temperature sensors. Marengo *et al.* reported that LIG fabricated on PI substrates exhibited a temperature coefficient of resistance (TCR) around $-0.11\%\ ^{\circ}C^{-1}$,[97] which surpasses that of free-standing carbon nanotube networks ($-0.07\%\ ^{\circ}C^{-1}$)[98] but is slightly lower than graphene flakes ($-0.18\%\ ^{\circ}C^{-1}$).[99]

Beyond PI, other carbon precursors have also been utilized in the fabrication of LIG-based temperature sensors. Yang *et al.* developed LIG temperature sensors on Kevlar textiles, which exhibited a negative TCR of $-0.068\%\ ^{\circ}C^{-1}$ within a temperature range of 30–60 °C, with response and recovery times of 24.2 s and 27.5 s, respectively.[70] The exceptional thermal stability of both LIG and Kevlar enabled these sensors to maintain consistent performance under vacuum conditions (10^{-3} Torr) and repeated thermal cycling between −20 °C and 60 °C for approximately 40 hours. These characteristics highlight the potential of LIG/Kevlar sensors for demanding applications, such as smart spacesuits and telescopes operating in extraterrestrial environments. Moreover, the high thermal conductivity of LIG is advantageous for heat dissipation in space, where convective heat transfer is negligible. Remarkably, LIG temperature sensors have been successfully fabricated on natural substrates, such as wood and leaves (Fig. 7a).[29] Leaf-derived LIG temperature sensors demonstrated a TCR of $-0.08\%\ ^{\circ}C^{-1}$, with rapid response and recovery times of 7.0 s and 6.2 s, respectively. These sensors, crafted from natural materials, can be

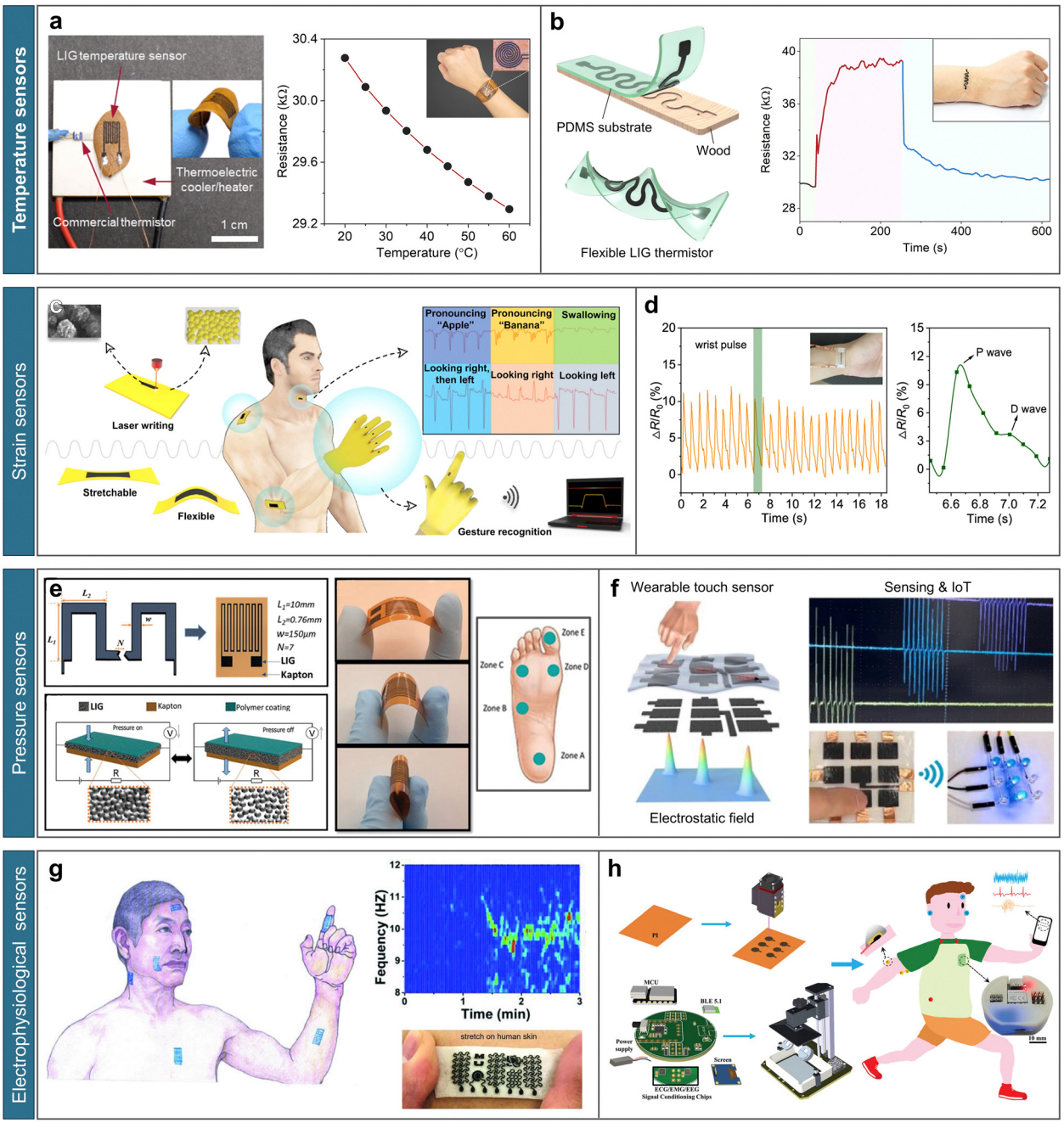

Fig. 7 (a) Left: Photograph of a LIG temperature sensor fabricated on a leaf and the experimental setup for performance evaluation. Right: Resistance–temperature response of the sensor over the range of 20–60 °C. Reproduced with permission.[9] Copyright 2019, Wiley-VCH Verlag. (b) Left: Transfer process of LIG from wood to a PDMS substrate. Right: LIG/PDMS temperature sensor used for monitoring human body temperature. Reproduced with permission.[63] Copyright 2021, Elsevier. (c) Application of a LIG-based strain sensor for tracking muscle movements and human motions. Reproduced with permission.[103] Copyright 2022, Springer Nature. (d) Left: Real-time signal captured by the F-LIG/PDMS sensor for wrist pulse monitoring. Right: Enlarged view of the shaded region showing distinct P-wave and D-wave components. Reproduced with permission.[75] Copyright 2024, Springer Nature. (e) Left: Schematic design and working principle of LIG-based pressure sensors. Middle: Photographs demonstrating the sensor's mechanical flexibility. Right: Placement of LIG pressure sensors on the foot for dynamic pressure mapping. Reproduced with permission.[20] Copyright 2020, John Wiley & Sons, Inc. (f) A triboelectric touch sensor comprising a 3 × 3 LIG electrode array, capable of wirelessly controlling LEDs. Reproduced with permission.[18] Copyright 2024, American Chemical Society. (g) Left: Schematic illustration of sensor placement on various body parts (forehead, chest, forearm, face, neck, and finger) for monitoring electrophysiological signals such as EEG, ECG, and EMG. Top right: Recorded alpha rhythm signal from the forehead. Bottom right: Photograph of the sensor. Reproduced with permission.[21] Copyright 2018, Wiley-VCH Verlag. (h) Fabrication process, concept, and photograph of a three-in-one portable electronic platform designed for simultaneous measurement of EEG, ECG, and EMG signals. Reproduced with permission.[116] Copyright 2023, Wiley-VCH Verlag.

seamlessly integrated into furniture or decorative elements, facilitating unobtrusive environmental temperature monitoring in indoor settings.

In contrast to the NTC behavior commonly observed in LIG temperature sensors, Le *et al.* introduced an LIG composite temperature sensor exhibiting a positive temperature coefficient (PTC), where the electrical resistance increases with rising temperature.[63] In this approach, LIG initially fabricated on wood was transferred onto a flexible PDMS substrate (Fig. 7b). Graphene typically shows a negative thermal expansion coefficient (-8.0 ± 0.7 ppm K^{-1}),[100] meaning it contracts upon heating, whereas PDMS expands with temperature, having a positive thermal expansion coefficient (309.6 ± 6.9 ppm K^{-1}).[101] Upon heating, the contraction of LIG islands and simultaneous expansion of the PDMS substrate cause a substantial reduction in the physical contacts between LIG domains. This phenomenon dramatically increases the overall electrical resistance. Due to these contrasting thermal expansion characteristics, the LIG composite sensor demonstrates an exceptionally high temperature sensitivity with a TCR of approximately 5.73% $^{\circ}C^{-1}$. The enhanced sensitivity of this LIG composite sensor makes it highly effective for precise and real-time monitoring of human body temperature in wearable health monitoring platforms.

Overall, LIG temperature sensors are promising candidates for the widespread adoption of carbon-based temperature sensing technologies due to low cost, high sensitivity, and mechanical flexibility. However, their susceptibility to environmental humidity makes water-resistant encapsulation essential for practical applications.

4.1.2. Strain sensors. The human body generates various mechanical signals that are valuable not only for assessing health conditions but also for enabling control of external devices, such as prosthetics or robotics. Examples include chest expansion and contraction during breathing, pulses at the neck or wrist, joint movements, and laryngeal vibrations during speech. To continuously and precisely monitor these signals, the use of flexible strain sensors is essential. LIG features a foam-like structure that deforms under external forces, resulting in a change in electrical conductivity, known as the piezoresistive effect. Consequently, LIG has been effectively employed as strain sensing material, with experimental results demonstrating that LIG-based strain sensors exhibit excellent performance and durability compared to other graphene-like materials.

One of the earliest studies exploring LIG for strain sensing was reported by Luo *et al.* in 2016.[102] They fabricated LIG strain sensors directly on PI substrates in ambient air using a CO_2 laser. They found that laser power significantly affected the piezoresistive sensitivity of the LIG strain sensors. Upon optimization, they achieved a gauge factor (GF), defined as the ratio of relative resistance change to applied mechanical strain, of approximately 112. Similarly, Carvalho *et al.* utilized a 355 nm diode-pumped Nd:YVO_4 pulsed laser to fabricate LIG strain sensors on PI substrates,[35] reporting a GF as high as 125, closely aligning with Luo *et al.*'s findings.[102] Therefore, LIG strain sensors on PI substrates emerge as a sensitive and inexpensive alternative to conventional metal foil strain gauges, with demonstrated applications in heart rate monitoring, gesture recognition, and human–machine interfaces (HMIs).

Although LIG sensors exhibit relatively high sensitivity, their maximum tensile strain is limited to about 1.5%, as reported in the studies mentioned above, primarily due to the inherent properties of the PI substrate. This limitation restricts their applicability as wearable devices. Several strategies have been proposed to overcome this issue. Wang *et al.* developed stretchable LIG-based strain sensors from a carbon precursor consisting of PI and PDMS (Fig. 7c).[103] These stretchable LIG strain sensors exhibited a GF of approximately 30 and could withstand mechanical strain of over 15% at a PI : PDMS ratio of 1 : 2. By altering the ratio to 1 : 4, the GF increased up to 75, though the maximum tensile strain decreased to about 4%. Due to their wide working range, LIG strain sensors are well-suited for wearable applications, such as monitoring joint movements for gesture recognition. Besides, LIG can initially be fabricated on rigid substrates and subsequently transferred onto elastomeric substrates such as PDMS[75,104,105] or PU[19] to dramatically enhance stretchability. For example, LIG transferred onto a PDMS substrate exhibited a linear strain response with a working range of up to 100% and a GF of 3.45.[104] Given their high sensitivity and conformal attachment capability on diverse areas of human skin, these sensors hold significant potential for monitoring vital physiological signals (Fig. 7d) such as heart rate, respiratory rate, and facial emotional expressions.

Beyond these applications, LIG strain sensors can monitor muscle movements in the throat for distinguishing various activities (*e.g.*, swallowing, speaking), or detecting minute vibrations for word and sentence recognition.[106] Such signals can be utilized for HMIs, anti-interference voice recognition, or security applications. Besides detecting throat vibrations, LIG has also been identified to exhibit sound generation capabilities based on the thermoacoustic effect.[107] Tao *et al.* developed an artificial throat device capable of functioning both as a sound detector and generator, enabling mute individuals to convert throat vibrations such as humming, coughing, or screaming into intelligible audio signals through pattern recognition and machine learning techniques. By detecting resistance changes induced by vocal cord vibrations, the system classifies and translates these signals into specific outputs, demonstrating its potential for assistive voice technologies.

In addition, LIG strain sensors can be directly fabricated on textiles, enabling seamless integration into everyday clothing for natural and continuous monitoring of human activity.[55] Beyond daily use, these sensors can also be incorporated into protective garments such as firefighter uniforms or spacesuits, thanks to the superior thermal stability of LIG.[70,108]

Compared to conventional metal strain gauges, which typically have a GF of around 2 and a working strain range of up to 1%, LIG-based strain sensors exhibit significantly higher sensitivity and stretchability. The ability to engineer microstructures and form composites with a wide range of materials enables

tunable performance parameters across a broad range, making them highly adaptable for diverse applications.

4.1.3. Pressure and tactile sensors. Another common type of physical sensor is the pressure sensor, whose electrical signal changes in response to applied pressure. Although various sensing mechanisms are available, the piezoresistive effect is the most prevalent, similar to that used in strain sensors. Kaidarova *et al.* demonstrated a LIG-based pressure sensors on PI substrates using a CO_2 laser (Fig. 7e).[20] The structure of this LIG pressure sensor consists of a LIG film with a thin protective layer of polymethyl methacrylate (PMMA) coated on top. The sensing mechanism relies on the piezoresistive effect where external pressure deforms the porous, low-modulus, three-dimensional graphene network, decreasing interlayer spacing and enhancing the contact area between graphene flakes. This deformation increases the number of conductive pathways, resulting in a measurable decrease in electrical resistance. Sensitivity can be tailored by altering the geometry of the meander-shaped electrodes, while the rigid PMMA layer facilitates stress transfer and provides mechanical protection. The fabricated sensor exhibited a linear pressure response with a sensitivity of 1.23×10^{-3} kPa^{-1}, a high resolution (detection limit of 10 Pa), and an exceptionally broad dynamic range exceeding 20 MPa. Furthermore, the device demonstrated stable performance over 15 000 loading cycles (over 100 hours) without noticeable degradation. This LIG pressure sensor has been effectively utilized in heart rate monitoring and tactile sensing for gait analysis.

To investigate the impact of elastomer encapsulation, Shin *et al.* studied various elastomeric encapsulation layers, including PDMS (with base-to-curing-agent ratios of 5 : 1, 10 : 1, and 20 : 1) and Ecoflex 1 : 1.[109] The curing agent ratios were adjusted to control the mechanical properties of the elastomers, and their thickness was standardized at 180 μm *via* spin-coating. All sensors showed increased resistance under applied pressure. The Ecoflex-encapsulated sensor exhibited the highest sensitivity (0.241% at 400 kPa), attributed to its lower Young's modulus (0.073 MPa). Conversely, stiffer encapsulants such as PDMS 5 : 1 (1.75 MPa) had substantially lower sensitivity. Response time evaluations revealed that higher modulus materials resulted in faster responses, with the PDMS 5 : 1 sensor achieving the shortest response time of 505 ms at 100 kPa. Mechanical stability tests over 3000 cycles indicated minimal degradation for all sensors. However, sensors with softer encapsulants (Ecoflex and PDMS 20 : 1) initially experienced signal drift due to irreversible graphene deformation, stabilizing after approximately 1000 cycles. Environmental stability tests at 85 °C over 48 hours confirmed negligible baseline resistance drift or sensitivity loss, emphasizing the critical role of encapsulation material selection in optimizing sensor sensitivity, response speed, and durability.

Besides, composite materials incorporating LIG have also been explored to enhance pressure sensing performance. For instance, Li *et al.* fabricated an MXene/LIG heterostructure through laser irradiation of an MXene/polyamic acid (PAA) composite.[110] The resulting LIG composite sensor exhibited exceptional sensitivity (20 kPa^{-1}) and a 567% improvement over bare LIG sensors. This significant enhancement results from conductive pathways formed by MXene nanosheets integrated within the LIG matrix and stable chemical bonding at the MXene–LIG interface. Furthermore, the sensor demonstrates a wide detection range (up to 80 kPa), rapid response and recovery times (42 ms and 28 ms, respectively), and robust durability over 4000 cycles. Due to its superior sensitivity, this sensor is well-suited for voice, pulse, and respiration monitoring.

Remarkably, Yang *et al.* introduced a self-powered LIG-based pressure sensor utilizing the triboelectric effect rather than the conventional piezoresistive mechanism (Fig. 7f).[18] Consisting of an LIG electrode sandwiched between two silicone elastomer layers, this sensor operates through a four-stage contact-separation cycle. Initially, with no contact, negatively charged silicone induces positive charges in the LIG. Approaching contact with a positively charged object partially offsets this effect. Upon full contact, electrostatic fields neutralize, discharging induced charges in the LIG. Removing contact restarts the induction, generating measurable transient electrical signals as voltage or current. This triboelectric sensor shows high sensitivity, rapid response (<10 ms), and exceptional durability over more than 15 000 cycles, even under repeated bending. It maintains reliability across diverse touch frequencies and pressure levels and can also function as an energy harvester, achieving a peak power output of 20.3 μW. For wearable applications, optimizing the thickness of the silicone encapsulation, particularly the bottom layer, substantially enhances signal strength, highlighting the significance of mechanical design in the performance of triboelectric sensors.

4.1.4. Electrophysiological sensors. Continuous monitoring of electrophysiological signals from the heart (ECGs), muscles (EMGs), and brain (electroencephalograms, EEGs) is crucial for advancing wearable electronics, particularly for health monitoring and HMIs. ECGs provide vital information on cardiac health, helping to detect normal rhythms and abnormalities such as arrhythmias.[111] EEGs offer detailed insights into brain activity, aiding in understanding normal neural functions and diagnosing neurological disorders.[112] EMGs are indispensable for diagnosing neuromuscular diseases and controlling devices such as prosthetics.[113]

LIG and graphene derivatives offer notable advantages as electrode materials for electrophysiological monitoring.[114] Their excellent electrical conductivity, large surface area, and mechanical flexibility enable conformal contact with the skin, allowing for stable signal acquisition without the use of conductive gels. Moreover, graphene-based electrodes demonstrate low noise, high biocompatibility, and compatibility with scalable fabrication techniques, making them well suited for next-generation wearable and long-term bioelectronic applications.

Sun *et al.* demonstrated that LIG is highly effective for fabricating electrodes used in electrophysiological sensing (Fig. 7g).[21] LIG electrodes were initially patterned on PI substrates *via* CO_2 laser irradiation and subsequently transferred onto partially cured substrates made from a silicone elastomer

mixed with sugar powder at a 1 : 2 weight ratio. After curing at room temperature and dissolving the sugar in deionized water, flexible and gas-permeable substrates featuring LIG electrodes suitable for EEG, ECG, and EMG recordings were successfully obtained. These electrodes showed a contact impedance of around 17 kΩ at 100 Hz (contact area: ~0.3 cm^2), comparable to traditional gel electrodes (~12 kΩ at 100 Hz; contact area: ~2.6 cm^2) and significantly lower than free-standing gold nanomesh electrodes (~140 kΩ at 100 Hz).[115] Practical tests involved attaching these electrodes to a volunteer's forehead for EEG, chest for ECG, and various muscles (forearm, face, neck, fingers) for EMG measurements. The recorded signal quality closely matched that of conventional silver/silver chloride (Ag/AgCl) gel electrodes.

Dallinger *et al.* simplified the fabrication process by using commercially available medical-grade PU, known for its excellent breathability, as the transfer substrate for LIG-based EMG sensors.[19] These sensors featured circular LIG electrodes directly applied to the forearm without prior skin preparation. Comparative tests with standard Ag/AgCl gel electrodes revealed that the LIG sensors achieved a high signal-to-noise ratio and stable performance equivalent to conventional electrodes. Subjects wore the electrodes continuously for three days while engaging in typical daily activities, including lab work, exercise, showering, and sleeping. Owing to their thinness, flexibility, and breathability, these electrodes caused minimal discomfort, and no skin irritation or allergic responses were reported upon removal.

Further advancements include the development of portable and multimodal data acquisition systems capable of simultaneous EEG, ECG, and EMG recording (Fig. 7h).[116] Such integrated devices include all necessary components (sensors, power supply, wireless communication modules, and protective housing) within a compact form factor weighing approximately 22 grams and costing around $25. This versatile, portable system has shown promise in real-world applications, including fitness monitoring, medical diagnostics, and various HMI scenarios.

4.2. Chemical and biochemical sensors

LIG electrodes have been explored for applications in clinical diagnostics, personalized healthcare, and real-time health monitoring. Their surfaces can be functionalized with highly specific bioreceptors such as antibodies, enzymes, aptamers, and imprinted polymers to enhance target selectivity. These modifications enable LIG-based biosensors to detect a wide range of health-related biomarkers, such as ions, cytokines, metabolites, nucleic acids, and pathogens.

4.2.1. Ion detection. LIG has rapidly become a universal transducer for ion sensors due to its facile, mask-free fabrication, high conductivity, and tunable surface chemistry. Across potentiometric, voltammetric, and chemiresistive modalities that produce electrical signals proportional to analyte concentration, LIG electrodes paired with tailored ionophores (polyvinyl chloride membranes, metal oxides, Prussian blue analogues), conductive polymers (polyaniline (PANI), poly(3,4-ethylenedioxythiophene):polystyrene sulfonate (PEDOT:PSS)), or simple electrochemical activation have yielded near-Nernstian responses, low micromolar to nanomolar detection limits, and robust operation in complex matrices such as sweat, food extracts, natural waters, and soil leachates.

Lin's group demonstrated a flexible tri-channel LIG sensor on PI for wearable sweat analysis (Fig. 8a).[117] They coated LIG with PEDOT:PSS as an ion-to-electron transducer and integrated polyvinyl chloride (PVC) membranes with valinomycin for K^+, a Na^+ ionophore, and electrodeposited PANI for pH. By tuning laser power and raster speed, they achieved highly porous LIG sensors that yielded near-Nernstian sensitivities (51.5 mV per decade for pH, 45.4 mV per dec for Na^+, 43.3 mV per dec for K^+) and linear detection over 0.1–100 mM. The device showed good selectivity and mechanical flexibility, enabling real-time on-body monitoring.

In contrast, LIG potentiometric ion-selective electrodes have also been developed for environmental ions. Gomes's group created a hydrophobic LIG using a double-lased PI to eliminate water-layer effects under solid-contact NO_3^- membranes (Fig. 8b).[118] The resulting NO_3^- LIG-ISE showed a −58.2 mV per decade response and LOD ~ 6.0 μM, with stable operation validated against EPA methods in lake water. Likewise, Gomes's group used hydrophobic LIG (surface-treated to repel water) for a NO_2^--selective ISE.[119] Their device displayed a 59.5 mV per decade slope and an extended linearity of 10^{-5}–10^{-1} M (LOD ~ 0.3 mg L^{-1}) for nitrite, enabling direct measurement in meat extracts.

For heavy-metal ions, LIG's high surface area has been leveraged in stripping voltammetry. Raouafi's group optimized laser parameters to create LIG sensors for Pb^{2+} and Cd^{2+} detection without any added metal modifiers.[120] 3D-porous LIG electrodes, generated by direct laser writing on PI, inherently pre-concentrate metal ions by physical adsorption within the graphene network. In square wave anodic stripping voltammetry (SWASV), their LIG sensors gave sensitivities of 0.45 μA (ppb^{-1} cm^{-2}) (Cd^{2+}) and 0.93 μA (ppb^{-1} cm^{-2}) (Pb^{2+}), linear ranges of 25–1000 ppb (Cd^{2+}) and 10–500 ppb (Pb^{2+}), and LODs 6.1 ppb (Cd^{2+}) and 3.0 ppb (Pb^{2+}). The elimination of metal-film deposition reduces complexity and cost. Separately, Jaramillo-Botero's group electrodeposited a bismuth (Bi) film onto LIG for Al^{3+} detection.[121] The Bi-LIG electrodes facilitate Al^{3+} pre-concentration and stripping. SWASV yields a linear 1.07–300 ppm range and LOD of 0.34 ppm, matching ICP-OES results within 98% accuracy, and was unaffected by coexisting Pb^{2+}, Cd^{2+}, or Cu^{2+}, highlighting its agronomic applicability. These LIG-based heavy-metal sensors exploit either the intrinsic porosity (no added reagents) or the combination of LIG with a redox-active film (Bi for Al^{3+}) to achieve ppb–ppm sensitivity.

Finally, Verma's group reported a chemiresistive LIG sensor for Hg^{2+} that relies on metal–ligand complexation rather than electrochemistry.[122] They laser-etched microchannels into a phenol-formaldehyde film to form LIG patterns and embedded Cu nanoparticles as Hg^{2+}-binding receptors. This capillary-driven LIG film exhibited a fast resistive response to Hg^{2+}+, with two linear regimes (2–30 ppb and 0.03–20 ppm) and high

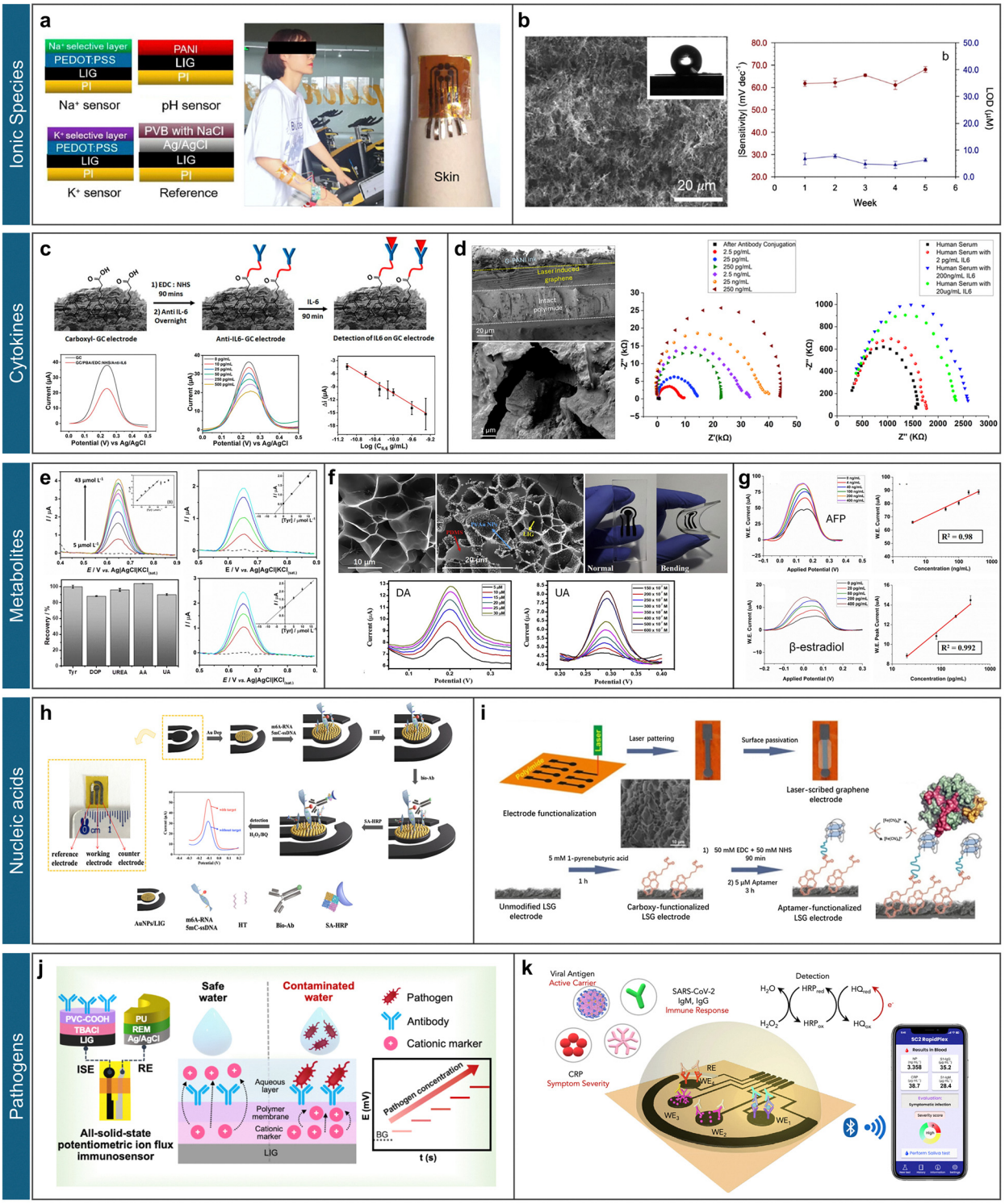

Fig. 8 (a) Schematic of a LIG-based sensor for continuous sweat analysis, enabling simultaneous monitoring of pH, Na^+, and K^+ concentrations. The sensor includes individual ion-selective electrodes and an integrated Ag/AgCl reference electrode. Reproduced with permission.[117] Copyright 2022, MDPI. (b) SEM image of LIG following a second laser treatment, revealing a roughened, flattened, and hydrophobic surface. Contact angle measurement with DI water confirms hydrophobicity, designed to minimize water-layer effects under solid-contact NO_3^- selective membranes. Long-term performance shows stable sensitivity and LOD over five weeks of storage in surface water. Reproduced with permission.[118] Copyright 2022, Springer Nature. (c) Schematic of LIG surface modification and IL-6 capture. Graphs show baseline *vs.* modified response, as well as linear response with target. Reproduced with permission.[123] Copyright 2021, MDPI. (d) Cross-sectional view of the sensor showing three distinct regions and top view of porous G-PANI ink showing flat graphene sheets held together by PANI. EIS response obtained from LIG/G-PANI immunosensor with an increased IL-6 antigen concentration from 0.002 to 20 pg mL^{-1} in buffer and in human serum sample. Reproduced with permission.[124] Copyright 2024, American Chemical Society. (e) Baseline-corrected DPV recorded for increasing concentrations of Tyr in the range of 5–43 μmol L^{-1} and recovery data of Tyr in the presence

of contaminants. Additional graph shows DPV measurement of Tyr in buffer and urine samples. Reproduced with permission.[126] Copyright 2022, Wiley-VCH Verlag. (f) FESEM images of LIG/PDMS electrode and modified Pt-AuNPs/LIG/PDMS electrode. DPV data for DA and UA in 0.1 M PBS buffer. Reproduced with permission.[130] Copyright 2019, Elsevier. (g) DPV current response and linear response of immunosensor at varying concentrations of AFP and β-estradiol. Reproduced with permission.[125] Copyright 2024, MDPI. (h) Schematic illustration of LIG biosensor modification process for nucleic acid methylation detection. Reproduced with permission.[25] Copyright 2024, Royal Society of Chemistry. (i) Schematic diagram of preparing LIG-based aptamer interdigitated array electrodes. Reproduced with permission.[81] Copyright 2017, American Chemical Society. (j) Schematic illustration of the fabrication steps and operating principle of an all-solid-state potentiometric ion flux immunosensor targeting *Escherichia coli* and *Salmonella enterica*. Reproduced with permission.[138] Copyright 2024, American Chemical Society. (k) Wireless graphene-based electrochemical platform for rapid, multiplexed detection of SARS-CoV-2 in blood and saliva samples. Reproduced with permission.[26] Copyright 2020, Cell Press (Elsevier).

sensitivities (0.64 Ω ppb^{-1} and 66.92 Ω ppm^{-1}) and LOD of 2.41 ppb and 0.47 ppm. This chemiresistive mode, distinct from stripping voltammetry, achieved sub-ppb Hg detection *via* simple resistance change.

In summary, these LIG sensors each pair a specific sensing element (ionophore membrane, polymer, metal film, or surface activation) with LIG's 3D conductive scaffold. The result is highly sensitive, low-cost sensing: near-Nernstian ion electrodes rival standard ISEs, and unmodified LIG platforms enable multi-analyte voltammetry with performance comparable to or exceeding conventional electrodes. The novel aspects range from hydrophobic laser treatments for stable ion-to-electron transduction to simple polarization for bioanalytical activation. Table 1 compares the designs and performances of these LIG-based sensors.

4.2.2. Cytokine detection. Cytokines are critical signaling molecules within the immune system. They are key players in regulating inflammation, mediating immune responses, and participating in a broad array of cell signaling pathways. However, aberrant cytokine expression is closely linked to the pathogenesis of numerous diseases, including autoimmune disorders, infections, cancer, and chronic inflammatory conditions.

For the electrochemical detection of cytokines, Iacopino's group functionalized LIG electrodes with 1-pyrenebutyric acid, 1-ethyl-3-(3-dimethylaminopropyl) carbodiimide, and *N*-hydroxy succinimide, followed by antibody immobilization (Fig. 8c).[123] This sensor platform enabled the linear detection of interleukin-6 (IL-6) in phosphate-buffered saline (PBS) across a concentration range of 10–500 pg mL^{-1}, achieving a limit of detection (LOD) of 5.1 pg mL^{-1}, which is comparable to existing commercial assays. The sensors also demonstrated robust shelf-life stability, retaining performance for up to six weeks at 4 °C. Building upon this, Nazmul Islam's group incorporated a graphene-PANI (G-PANI) conductive ink to further enhance the electrochemical performance of the LIG-based sensor for IL-6 detection (Fig. 8d).[124] The increased conductivity and surface area provided by the G-PANI composite enabled an improved LOD of 2.62 pg mL^{-1}.

In hepatocellular carcinoma diagnostics, Tabassum *et al.* utilized a similar LIG/G-PANI sensor configuration for the detection of alpha-fetoprotein (AFP).[125] In PBS, the sensor exhibited a linear detection range of 4–400 ng mL^{-1} and an LOD of 1.15 ng mL^{-1}. The stability of the sensor was evaluated using differential pulse voltammetry (DPV), with ten consecutive measurements yielding a low relative standard deviation of 1.66%, indicating excellent reproducibility and operational reliability.

Functionalization of LIG electrodes with specific antibodies enables selective detection, while the incorporation of G-PANI composites enhances both conductivity and sensitivity. Compared to traditional methods such as ELISA, these sensors provide comparable or improved sensitivity, faster response times, and are well-suited for portable, point-of-care applications, making them promising tools for early disease diagnosis and monitoring.

4.2.3. Metabolite detection. As the body experiences different physiological, environmental, and pathological states, corresponding changes are reflected in metabolite levels. These changes serve as sensitive biomarkers for early disease detection, prognosis, and monitoring of treatment responses across a wide range of conditions, including cancer, cardiovascular disease, diabetes, and infectious diseases.

Tyrosine, dopamine and uric acid. Tyrosine (Tyr) is an important bio-precursor in human blood, and its presence in urine may indicate potential liver- or thyroid-related disorders. In 2022, Muñoz's group developed a LIG sensor on PI substrate for Tyr detection (Fig. 8e).[126] Using DPV, the sensor demonstrated good linear response from 5–30 μmol L^{-1}, with an LOD of 1.5 μmol L^{-1}. To simulate biofluid conditions, Tyr was spiked into a solution containing common urinary components, including dopamine (DA), uric acid (UA), and ascorbic acid (AA), in a 1 : 1 ratio. The LIG sensor exhibited good selectivity, achieving Tyr recovery rates exceeding 88%. In another study, Iacopino's group utilized cork as a substrate for LIG fabrication, enabling detection of Tyr in the range of 5–150 μM with an LOD of 3.03 μM without extensive sensor modification.[127] The same sensor was later integrated into a microfluidic system and tested in artificial sweat, where it achieved an extended upper detection limit of 250 μmol L^{-1} and a comparable LOD of 3.75 μmol L^{-1}.

DA is a critical neurotransmitter and hormone routinely monitored in blood and brain tissues for the diagnosis and management of neurological disorders, including Parkinson's disease, schizophrenia, and attention deficit hyperactivity disorder (ADHD). Shinde and Slaughter reported the use of LIG modified with $Nb_4C_3T_x$ MXene, polypyrrole (PPy), and iron nanoparticles (FeNPs), achieving linear DA detection from 1 nM to 1 μM with an LOD of 70 pM.[128] Similarly, Roy's group modified electrodes with $Ti_3C_2T_x$ MXene and NiO nanoparticles, reaching LODs of 1.97 μM for DA, 16 μM for AA, and 0.78 μM for UA.[129] In a simpler approach, Hui *et al.*

Table 1 Performance of LIG-based sensors for ion detection

Analyte	Detection method	Electrode material	Sensing element	Test sample	Linear range	Sensitivity	LOD	Ref.
pH, Na^+, K^+	Potentiometric	LIG	PVC membranes	Sweat	0.1–100 mM (Na^+, K^+)	51.5 mV per dec (pH); 45.4 mV per dec (Na^+); 43.3 mV per dec (K^+)	—	117
NO_3^-	Potentiometric	Hydrophobic LIG	PVC membrane	Lake water	$10^{-3.5}$–10^{-1} M	−58.17 mV per dec	6.01 μM	118
NO_2^-	Potentiometric	Hydrophobic LIG	PVC membrane	Meat extracts	10^{-5}–10^{-1} M	59.5 mV per dec	7.2 μM	119
Cd^{2+}, Pb^{2+}	SWASV	LIG	—	Ore and tap water	Cd: 25–1000 ppb, Pb: 10–500 ppb	0.45 (Cd), 0.93 (Pb) μA (ppb^{-1} cm^{-2})	6.13 (Cd), 2.96 (Pb) ppb	120
Al^{3+}	SWASV	Bi-plated LIG	Electrodeposited Bi film	Soil extract	1.07–300 ppm	—	0.34 ppm	121
Hg^{2+}	Electrical resistance	Cu-NP/LIG	Cu-NP	Water	2–30 ppb 0.03–20 ppm	0.64 Ω ppb^{-1} 66.92 Ω ppm^{-1}	2.41 ppb 0.47 ppm	122

enhanced LIG electrodes by electroplating with platinum and gold nanoparticles (Pt/Au NPs), enabling DA detection in the range of 95 nM to 30 μM with an LOD of 75 nM (Fig. 8f).[130]

UA, a normal metabolic waste product, serves as a key biomarker for health conditions such as gout, hyperuricemia, neuropathy, type 2 diabetes, and renal dysfunction. In 2021, Salama's group introduced an electrochemically activated LIG sensor modified with gold nanoparticles (AuNPs), allowing simultaneous detection of UA and DA with LODs of 0.6 μM and 0.8 μM, respectively.[131] In another approach, Bhattacharya *et al.* utilized bare two-electrode paper-based LIG devices and employed SWASV and chronoamperometry (CA).[132] Despite minimal sensor modification, these devices achieved a UA sensitivity of 24.35 ± 1.55 μA μM^{-1} and an LOD as low as 41 nM, although measurements were conducted in controlled, optimized aqueous solutions.

Thrombin, ctnI, and 17β-estradiol. Clinically important protein and hormone biomarkers like thrombin, cardiac troponin-I (cTnI), and 17β-estradiol have emerged as important targets for sensor development due to their critical role in disease diagnostics. Thrombin, a key component in blood coagulation cascade, is associated with thrombotic disorders and cardiovascular diseases. Timely detection of thrombin is crucial for management of clotting abnormalities and its systemic effects. LIG-based sensors modified with copper–silver (Cu–Ag) nanoparticles and integrated with microfluidic channels have been developed to enhance aptamer immobilization and signal transduction.[133] These sensors demonstrate a linear detection range of 0.1–50 units per mL for thrombin, enabling sensitive quantification in physiological samples. Nanocomposite modification not only increases the active surface area but also improves electron transfer, resulting in robust sensor performance.

cTnI is the gold-standard biomarker for diagnosing myocardial injury and acute myocardial infarction. Its early detection is critical for accurate risk stratification and timely intervention in patients with suspected cardiac attacks. In a 2021 study by Salama's group, LIG electrodes were modified with the binary transition metal oxide $ZnFe_2O_4$ followed by aptamer immobilization *via* drop casting.[134] The resulting aptasensor exhibited a linear detection range of 1–10 pg mL^{-1} and achieved an LOD of 0.6 pg mL^{-1} in human serum.

Meanwhile, 17β-estradiol measurement is essential for diagnosing hormonal imbalances, monitoring fertility, and managing diseases such as breast cancer and autoimmune conditions. LIG sensors modified with PANI have been employed for the detection of both estradiol and AFP, achieving LODs of 0.96 pg mL^{-1} and 1.15 ng mL^{-1}, respectively.[125] These sensors demonstrated good linear ranges of 20–400 pg mL^{-1} for estradiol and 4–400 ng mL^{-1} for AFP in human serum (Fig. 8g).

Glucose and lactose. Glucose monitoring remains a fundamental aspect of diabetes management. Recent advances have focused on enhancing LIG-based sensors through the

deposition of metal nanoparticles (*e.g.*, Pt, Au, Ni) to increase electrocatalytic activity, along with the integration of conductive polymers or hybrid nanomaterials to improve electron transfer and biocompatibility.

In 2024, Malmali's group developed a $MnCO_3$/LIG composite electrode that achieved a high sensitivity of 2731.2 μA mM^{-1} cm^{-2} and an LOD of 2.2 μM.[135] This sensor demonstrated excellent recovery in blood serum samples, highlighting its clinical potential. In a separate study, James Pak's lab reported that Cu nanoparticle-modified LIG sensors were able to reach sensitivities up to 4000 μA mM^{-1} cm^{-2}, with LOD as low as 2 μM and broad linear ranges of 0.01–10 mM, covering physiological glucose concentrations.[136]

Further work from Yanxia Li's group demonstrated an LIG-based sensor integrating PEDOT and Au nanoparticles, with glucose oxidase (GOx) immobilized on the surface.[137] This sensor offered a sensitivity of 341.67 μA mM^{-1} cm^{-2} and an LOD of 0.2×10^{-5} M. In addition, non-invasive sweat glucose sensors based on CuO-embedded LIG within microfluidic systems have demonstrated rapid response times and wide detection ranges, advancing the potential for continuous, real-time glucose monitoring.[137]

Lactate monitoring is equally important, particularly for evaluating physical exertion and managing various medical conditions. LIG-based lactate sensors electroplated with bimetallic PdCu nanoparticles have demonstrated relevant sensitivity values reaching 872.08 μA mM^{-1} cm^{-2} and LOD as low as 0.167 μM in sweat.[136] In a high-performance dual biosensor platform, LIG electrodes modified with lactate oxidase exhibited a linear range within physiologically relevant concentrations, a sensitivity of 12.4 μA mM^{-1} cm^{-2}, and an LOD of 2.4 mM.[27]

LIG modified with MXenes, conductive polymers, and metal nanoparticles has been shown to significantly enhance the electrochemical surface area and electron transfer efficiency, resulting in lower detection limits and broader linear ranges. Compared to earlier LIG sensor designs, current LIG sensors can now achieve detection down to the picomolar level. Moreover, these functional modifications have demonstrated robust performance in real and complex biological matrices, representing a substantial improvement over many previously reported LIG and conventional sensors that were limited to simple aqueous systems or required extensive sample pretreatment.

4.2.4. Nucleic acid detection

m6A-RNA and 5mC-ssDNA. MicroRNA (miRNA) detection enables early and accurate diagnosis of various diseases such as cancer and cardiovascular disorders. Due to their stability in bodily fluids and disease-specific patterns, miRNAs serve as accessible and powerful biomarkers. Recent advances in detection technologies have facilitated the development of sensitive and non-invasive diagnostic tests, paving the way for improved disease monitoring and personalized treatment.

Recent studies have explored LIG-based biosensors for detecting epigenetic nucleic acid modifications, specifically N^6-methyladenosine RNA (m^6A-RNA) and 5-methylcytosine single-stranded DNA (5mC-ssDNA). In one such study, Wang's group described an LIG-based electrochemical immunosensor modified with gold nanoparticles, sulfhydryl-modified nucleic acid chains, biotinylated antibodies, and streptavidin-conjugated horseradish peroxidase.[25] The biosensor achieved an LOD of 2.81 pM for m6A-RNA and 9.53 pM for 5mC-ssDNA, with a linear detection range of 0.01–10 nM for both targets (Fig. 8h). The method demonstrated high selectivity, reproducibility across five electrodes (RSD 6.85%), and good stability in storage (RSD 9.42%) and consecutive scanning (RSD 2.08%). miRNA targets were successfully validated in spiked HeLa cell extracts, underscoring the sensor's diagnostic potential.

Compared to conventional nucleic acid detection techniques such as qPCR and ELISA-based methods, the LIG platform offers faster response times, lower detection limits, minimal sample preparation, and compatibility with miniaturized formats suitable for point-of-care applications. In addition, this approach exhibits significantly enhanced sensitivity and operational robustness, driven by the synergistic effects of nanomaterial integration and optimized biorecognition strategies. These advantages position LIG-based sensors as powerful, non-invasive tools for real-time, label-free nucleic acid diagnostics.

4.2.5. Pathogen detection. LIG has emerged as a versatile platform for the fabrication of high-performance biosensors targeting a broad spectrum of pathogens, leveraging its intrinsic high surface area, tunable porosity and conductivity, and facile surface chemistry for diverse transduction modalities.

For instance, Ruecha's group developed an all-solid-state potentiometric immunosensor for *Escherichia coli* and *Salmonella enterica*, in which PI-derived LIG electrodes were overcoated with a mixed PVC-COOH membrane doped with tetrabutylammonium chloride (TBACl) (Fig. 8j).[138] This creates a potentiometric interface where antibody–antigen binding modulates ion flux through the membrane, yielding wide linear ranges (0.1–10^5 CFU per mL) and low LODs (0.1 CFU per mL) for both *E. coli* and *Salmonella enterica* in water samples. In a separate approach, Gomes's group fabricated LIG electrodes functionalized with antibodies for electrochemical impedance sensing of *Salmonella enterica* in chicken broth.[139] Their label-free immunosensor achieved detection over 25–10^5 CFU per mL with an LOD of ~13 CFU per mL. In another work, Bonini's group used a LIG electrode covalently modified with an *E. coli*-specific DNA aptamer (P12-55) to detect *E. coli* in human urine by monitoring charge-transfer resistance.[140] This aptasensor showed a linear response between 1 and 10^3 CFU per mL.

Another innovative strategy targeted *Pseudomonas aeruginosa* indirectly by sensing its secreted redox-active metabolites. Ebrahimi's group used a simple electrodeposition step to decorate the graphene with molybdenum polysulfide (MoS_x), introducing abundant catalytically active sites for the selective electrochemical oxidation of *Pseudomonas*-derived phenazines.[141] The resulting MoS_x/LIG sensor achieves low LOD (0.19×10^{-6} M for pyocyanin (PYO), 1.2×10^{-6} M for phenazine-1-carboxylicacid (PCA)), specificity against non-phenazine producers, and long-term stability that enables real-time monitoring of biofilm growth.

Table 2 Performance of LIG-based sensors for pathogen detection

Analyte	Detection method	Electrode modification	Sensing element	Tested sample	Linear range	LOD	Ref.
Escherichia coli	Potentiometric	LIG + TBACl + PVC-COOH membrane	Anti-*E. coli* antibody	Groundwater/tap water	0.1–1 × 10^5 CFU per mL	0.1 CFU per mL	138
Escherichia coli	EIS	LIG (covalently functionalized)	Aptamer (P12-55)	Urine	1–1 × 10^3 CFU per mL	—	140
Salmonella enterica	Potentiometric	LIG + TBACl + PVC-COOH membrane	Anti-*Salmonella* Ab	Groundwater/tap water	0.1–1 × 10^5 CFU per mL	0.1 CFU per mL	138
Salmonella enterica	EIS	LIG	Anti-*Salmonella* Ab	Chicken broth	25–1 × 10^5 CFU per mL	13 ± 7 CFU per mL	139
Pseudomonas aeruginosa	SWV	MoSx-functionalized LIG	—	Brain heart infusion/cetrimide agar/wound simulating medium	1–100 μM	0.19 μM (PYO) 1.2 μM (PCA)	141
SARS-CoV-2	EIS	LIG + Pt nanoparticles	Biotinylated aptamer	Saliva	10–1 × 10^4 copies per mL	1.79 × 10^3 copies per mL	142
H1N1	CV	N-doped LIG + Au nanoparticles	Anti-H1N1 antibody	Serum/sweat/urine	0.01 fg mL^{-1}–10 ng mL^{-1}	0.004 fg mL^{-1}	143
Dengue	DPV	LIG	Dengue virus (DENV) antigen	Serum	25–2 × 10^4 ng mL^{-1}	17.41 ng mL^{-1}	144

Beyond bacteria, LIG platforms have been applied to viral targets. Gao's group leveraged mass-producible, flexible laser-engraved graphene (LEG) electrode arrays to achieve rapid, ultrasensitive, and multiplexed electrochemical detection of COVID-19 biomarkers (viral antigen NP, anti-spike IgM/IgG, and C-reactive protein (CRP)) in both blood and saliva (Fig. 8k).[26] This platform achieved rapid targeting with incubation times as short as one minute. In addition, Vanegas's group reported a LIG-based capacitive aptasensor for SARS-CoV-2 in saliva.[142] LIG channels patterned on PI were decorated with platinum nanoparticles to boost the gate capacitance. Biotinylated DNA aptamers with high affinity were immobilized *via* streptavidin linkage, and the resulting aptasensor achieved an LOD of 1.8 × 10^3 copies per mL in untreated saliva, with a dynamic range covering 10–1 × 10^4 copies per mL.

For influenza, Li's group created a label-free H1N1 immunosensor using N-doped LIG microelectrodes coated with electrodeposited Au nanoparticles and immobilized antibody.[143] *In situ* heteroatom N-doping within the graphene lattice enhanced conductivity and introduced edge defects that serve as electroactive sites. This sensor achieved an ultra-broad range (0.01 fg mL^{-1} to 10 ng mL^{-1}) and a LOD of 0.004 fg mL^{-1}.

In a study of dengue detection, Wongwiriyapan's group fabricated LIG electrodes and integrated them into a chip-based serological-detection platform.[144] Functionalization was achieved by immobilizing dengue virus antigen onto the LIG surface, enabling specific capture of anti-flavivirus (4G2) antibodies. The resulting device exhibited a broad linear working range (25–2 × 10^4 ng mL^{-1}), a low LOD (17.41 ng mL^{-1}).

Collectively, these studies underscore the remarkable adaptability of LIG for pathogen sensing through meticulous tuning of its surface chemistry, nanomaterial integrations, and bioreceptor architectures, LIG sensors deliver ultra-low detection limits, rapid response times, and robust performance in complex matrices, setting new benchmarks for point-of-care diagnostics across bacterial and viral threats. Table 2 compares the sensing mechanism, LIG modifications, biological probes, sample matrix, and performance metrics for several representative LIG-based pathogen sensors.

4.3. Gas sensors for breath analysis

4.3.1. Inorganic gas detection. The detection of hazardous and non-hazardous gases is of great significance for various applications, including air quality monitoring, hazard detection, health management, and diagnostics. This has driven substantial advancements in gas sensor technologies, particularly those based on LIG.[145–148] The analysis of exhaled breath, which dates back to Lavoisier's pioneering study of its chemical components in the 1780s,[149] has long been recognized as a valuable tool for health monitoring. In recent years, breath analysis has gained renewed attention as a non-invasive approach for clinical diagnostics and disease monitoring. It is worth knowing that human breath contains over 200 volatile organic compounds (VOCs), offering a rich source of diagnostic biomarkers.[149] The majority of exhaled human breath consists of nitrogen (N_2), oxygen (O_2), carbon dioxide (CO_2),

hydrogen (H_2), and inert gases, with concentrations 78.04%, 16%, 5%, and 0.9%, respectively.[149] In addition, inorganic compounds such as nitric oxide (NO_x), ammonia (NH_3), carbon monoxide (CO), and hydrogen sulfide, are also present at parts-per-million (ppm) or parts-per-billion (ppb) concentrations.[149]

Pristine LIG has been reported to intrinsically detect the composition of various gases, including O_2, CO_2, and N_2, based on its piezoresistive properties.[150] The temperature-sensitive conductivity of LIG filament scratched on PI allows the sensor to differentiate between vacuum and various gases *via* the convective cooling effect. The device exhibits a detectable response within 7–8 seconds and achieves stable readings within 30 seconds. The sensor demonstrated a significant response of about 250%, which is defined in eqn (1) to evaluate the sensing performance. R_t and R_0 are the resistance readings from the sensor in air and in the target gas.

$$S = \frac{\Delta R}{R_0} = \frac{R_t - R_0}{R_0} \quad (1)$$

Tuning the filament dimensions enabled more precise control of the Joule heating effect and improved repeatability. The optimized design could differentiate various gas types, although it suffered a loss in sensitivity of about 3.9%. Nevertheless, this approach required a continuous heat supply, leading to high energy consumption.

The second mechanism used in LIG gas sensors is the conventional chemiresistive sensing principle. This mechanism involves the adsorption and desorption of gas molecules on the sensing surface, which modifies the physical and chemical properties of the sensing material and results in a change in its electrical resistance.[146,151] By reading and analyzing the corresponding electrical signals, the concentration of the target gas can be determined. A wide range of 2D materials, from inert to chemically active and from semiconductive to metallic, with various thicknesses and elemental compositions, have shown strong potential for developing highly sensitive and portable sensors based on this mechanism.[148,152] The performance of LIG has also been studied to evaluate its capability in the application of health monitoring and diagnostics.[151] Owing to extremely high surface area and unique 3D porous structure, LIG can facilitate gas molecule absorption and provide high-energy binding sites.

Nitrogen oxides (NO_x) are well-established airway biomarkers in healthcare due to their vital role in respiratory and inflammation.[149,153] Measuring NO_x levels provides a non-invasive, rapid, and sensitive method to classify patients with respiratory diseases from healthy people (Fig. 9a). In asthma patients, the concentration of exhaled NO can reach several hundred ppb, which is tens of times higher than the typical levels found in healthy subjects (tens of ppb).[154–156] A gas sensor was developed using needlelike LIG to continuously monitor NO and NO_2 in human breath.[24] The concentration of NO_x is detected through a decrease in electrode resistance, caused by the extraction of electrons from the LIG surface due to NO_x adsorption. The bare LIG sensor enabled a LOD of 4.0 ppb, with response and recovery times of 134 and 388 seconds, respectively. However, the high relative humidity (RH) of human breath, typically between 50% and 95%, significantly compromises the sensor's performance. Therefore, the LIG sensing area was encapsulated between a soft elastomeric substrate and a gas-permeable PDMS layer (Fig. 9b and c). This configuration allows the sensor to function effectively in high-humidity environments, such as under the nose, while maintaining a strong response of 4‰, comparable to performance without the PDMS layer (Fig. 9d). On anatomically complex regions such as the philtrum, which contains a vertical groove, the flexibility of LIG provides a distinct advantage for gas sensing applications. Its excellent conformability enables close contact with the skin and stable performance under mechanical deformation, allowing for reliable sensing without disrupting natural facial movements or daily activities.

Besides pristine LIG, its functionalization with metal nanomaterials, semiconducting nanomaterials, and doped composites has been explored to improve gas sensing performance.[157,158] Various metal nanoparticles have been deposited on LIG to take advantage of its high surface area, porosity, and tunable surface chemistry, thereby improving its sensing capability. For hydrogen (H_2) sensing, palladium nanoparticles (PdNPs) were coated onto the LIG surface, which featured a turbinate-like structure that mimics the canine olfactory system.[158] PdNPs facilitate the detection *via* dissociative chemisorption governed by the spillover effect, resulting in a measurable change in the LIG sensing resistance. Platinum nanoparticles (PtNPs) were also post-synthesized on LIG for H_2 detection at room temperature.[159] The PtNPs smaller than 5 nm enhanced the intrinsic large specific surface area of the porous LIG structure, enabling a low LOD of 220 ppb with response and recovery times of 295 and 495 seconds, respectively. In another study, silver nanoparticles (AgNPs) were drop-cast onto LIG fabricated on a textile substrate made from a block copolymer.[23] The decoration of AgNPs increased both the surface area and conductivity of LIG, resulting in high sensitivity and selectivity for detecting NO_2, with a large response of −12‰ and fast response and recovery times of 40 and 291 seconds, respectively.

Aside from metal nanoparticle doping, the integration of semiconducting materials offers a promising strategy to enhance the gas sensing performance of LIG-based sensors. Molybdenum disulfide (MoS_2), known for its tunable band gap, high surface-area-to-volume ratio, and abundance of active sites, has been widely utilized in gas sensors, particularly in LIG-based platforms.[160–162] For NO_2 detection, several approaches using MoS_2 have been conducted. A sensing membrane composed of flowerlike MoS_2 nanostructures, sandwiched between interdigitated LIG electrodes, was able to detect NO_2 at a concentration as low as 2 ppm.[163] Its sensitivity and dynamic response were shown to strongly depend on the size and structural features of the MoS_2 nanostructures. A composite of MoS_2 with reduced graphene oxide (rGO) was reported to significantly boost the sensitivity of LIG in NO_2 sensing, achieving a LOD of 10 ppb at room temperature.[164] The MoS_2@rGO coating on LIG exhibited an improved

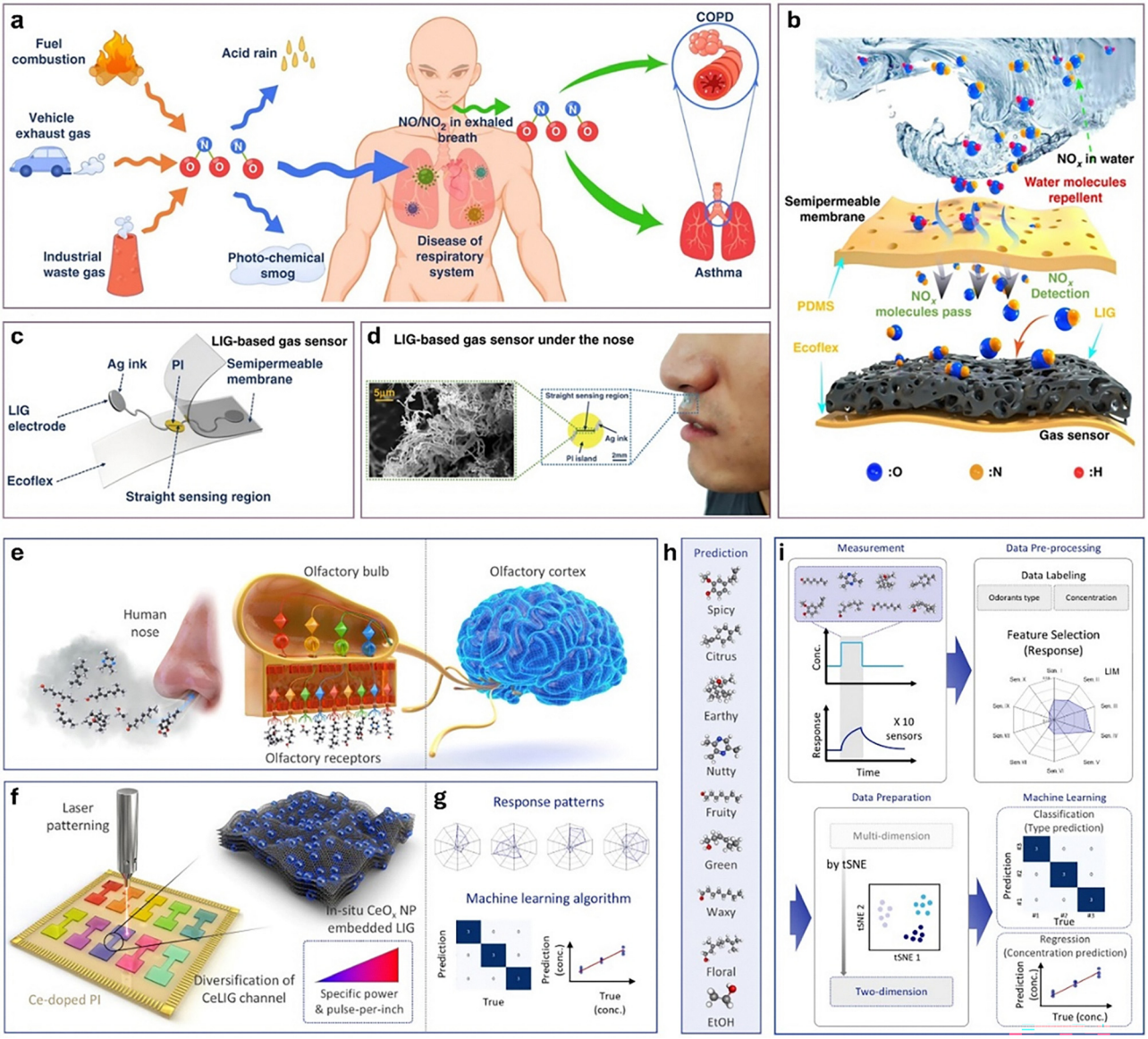

Fig. 9 LIG-based chemical sensors. (a)–(d) Moisture-resistant LIG sensor for NO/NO$_x$ detection. Reproduced with permission.[24] Copyright 2022, Springer Nature. (a) NO/NO$_x$ as a biomarker in human exhaled breath. (b) Sensing mechanism of the moisture-resistant LIG gas sensor. (c) Structural layout of the moisture-resistant and stretchable LIG gas sensor. (d) Optical and SEM images of the fabricated sensor. (e)–(i) Intelligent LIG-based olfactory system for odorant sensing. Reproduced with permission.[181] Copyright 2025, American Chemical Society. (e) Mechanism of human olfactory system. (f) LIG-based odorant sensing array. (g) Response patterns of sensing gases and machine learning algorithms. (h) Nine target odorant molecules. (i) Schematic illustration of data analysis based on machine learning.

sensitivity and a larger signal-to-noise ratio than the composite itself. The composite of LIG and Mxene has been investigated for detecting NO_2 in exhaled human breath and the surrounding environment.[165] This on-skin stretchable gas sensor showed opposite responses to NO_2 and NH_3, demonstrating a reliable detection and monitoring with a LOD of 5 ppb, and retaining performance over 1000 stretching and releasing cycles. Nevertheless, the response and recovery times were relatively long for realtime monitoring, reported as 7 and 32 minutes at 30 °C, and 6 and 19 minutes at 60 °C, respectively. To overcome this limitation, a semiconducting metal–organic material, Cu_3HHTP_2, showed its superiority in real-time monitoring with response and recovery times of 16 and 15 seconds, respectively (Fig. 9b).[166] The UV laser-patterned LIG functionalized with Cu_3HHTP_2, forming a lung-mimicking hierarchical microporous structure, enabling ultra-low LOD detection of 0.168 ppb without the need for catalytic heating or light activation.

Ammonia (NH_3) is a colorless and toxic gas with a pungent and suffocating odor that can be detected in exhaled human breath. The concentration of NH_3 tends to increase in individuals with kidney failure or liver dysfunction due to impaired ammonia metabolism and excretion.[167] Therefore, the measurement of NH_3 levels is important for health monitoring

and disease diagnosis. In 2018, the performance of pristine LIG for NH_3 sensing was investigated with and without heating.[168] Without heating, LIG-based gas sensors were able to detect NH_3 concentrations ranging from 75 to 400 ppm, with response and recovery times of 200 and 240 seconds, respectively. Although specific performance metrics under heating conditions were not detailed, the application of Joule heating at an optimized temperature of 70 °C was reported to improve the sensitivity and repeatability of the sensor.

The integration of LIG with conductive polymers has also been explored to enhance NH_3 sensing performance. PPy was synthesized on the LIG layer to detect NH_3 at room temperature.[169] As an electron-donating molecule, NH_3 transfers electrons to the PPy/LIG sensing layer upon interaction, reducing the hole concentration and consequently increasing the electrical resistance. The PPy/LIG composite was shown to improve the NH_3 sensing capability of bare LIG through a synergistic effect. However, it exhibited relatively long response and recovery times of 318 and 2775 seconds, respectively, compared to other reported sensing materials. Beyond PPy, various other conductive polymers have been extensively studied for gas sensing, particularly PANI, which has attracted significant attention due to its tunable conductivity, environmental stability, and strong interaction with target gas molecules.[170,171] A PANI-coated LIG sensor was developed for NH_3 detection.[172] Although the PANI/LIG composite exhibits a much lower detection limit of 2.38 ppb compared to 1 ppm for the PPy/LIG composite, it suffers from significantly longer response and recovery times of 18 minutes and 51 minutes, respectively. These results suggest that selecting between bare LIG and its composites for NH_3 sensing involves a trade-off: bare LIG typically offers faster response and recovery due to its high surface area and porous morphology, while LIG–conductive polymer composites provide higher sensitivity through stronger chemical interactions with NH_3, albeit at the cost of slower kinetics.

4.3.2. Volatile organic compound detection. In addition to significant advancements in inorganic gas sensing, LIG has also been applied to the detection of VOCs, which constitute a large proportion of human exhaled breath and are indicative of physiological conditions. One notable VOC is trimethylamine (TMA), which plays an important role in the development of gas sensing technologies for healthcare industry.[173,174] TMA is associated with the odor of certain infections, bad breath, and bacterial vaginosis. Zhao *et al.* developed a sensor using an LIG/Ag/ZnO composite capable of detecting TMA with a low detection limit of 5.6 ppb.[157] The study also compared the performance of pristine LIG and its composites with MoS_2, CuO, and Ag/ZnO in detecting NO_2, H_2S, and TMA. Each LIG composite exhibited programmable selectivity: LIG/MoS_2 for NO_2, LIG/CuO for H_2S, and LIG/Ag/ZnO for TMA. Furthermore, these composites exhibited self-heating capabilities, eliminating the need for interdigitated electrodes and a separate heater, while maintaining high sensitivity and rapid response.

Methane (CH_4) is produced by methanogens in the gut through anaerobic catabolism of dietary components and subsequently released *via* intestinal gas and pulmonary respiration.[175] The presence and concentration of CH_4 in breath are related to various gastrointestinal conditions, reflecting the expression of constipation, small intestinal bacterial overgrowth, colorectal cancer, and inflammatory enteritis.[175,176] Therefore, CH_4 detection in exhaled breath offers a promising approach for diagnosing related intestinal diseases. To address this, LIG-based gas sensors were developed by modifying the LIG surface with conductive polymer and metal nanocomposite for CH_4 detection (Fig. 9c).[22,177] PEDOT:PSS was incorporated to enhance sensitivity and facilitate electron transport. Methane was detected through an electrochemical signal generated by its redox activity on the electrode surface, which was further amplified by the introduction of a gold–platinum (Au–Pt) composite.[22] The sensor achieved a LOD of 0.36 ppm and demonstrated a linear detection range from 2 to 500 ppm when tested in a methane–air mixture.

Adhikari *et al.* developed a split-ring resonator sensor based on LIG, capable of detecting various VOCs without the need for an additional gas-sensitive interface.[178] The sensor operated by monitoring shifts in resonant frequency and amplitude, showing its ability to detect methanol (MeOH), ethanol (EtOH), acetone (ACE), and IPA. Among these, ACE exhibited the most significant response, with a wide detection range of 1–200 ppm and a linear correlation across different concentrations, even under various RH conditions. A unique aspect of this study was the utilization of electromagnetic field interaction between the resonator and target VOCs as the sensing mechanism, rather than relying on the conventional measurement of electrical resistance. To reduce environmental influence on VOC detection using LIG, tin monoxide (SnO) was integrated onto the LIG substrate.[179] This room-temperature chemiresistive sensor was able to detect MeOH, EtOH, IPA, and ACE with significantly faster response and recovery times of 50 and 5 seconds, respectively, much shorter than the above-mentioned split-ring resonator sensor (110 and 310 seconds). However, its limits of detection for MeOH and EtOH were 170 and 180 ppm, respectively, which were higher than those achieved by the pristine LIG sensor.

Beyond the impressive progress in single gas detection, LIG has also been employed for simultaneous detection of multiple VOCs. A virtual sensor array based on LIG interdigital electrodes and a MXene sensing layer was developed to function as an electronic nose (e-nose) to identify different types of VOCs and quantify their concentration.[180] Unlike traditional approaches that rely on resistance changes, this system obtained impedance spectra in response to different VOCs, including MeOH, EtOH, ACE, and IPA, and applied a machine learning algorithm to extract a fingerprint of eight representative parameters for classification. When integrated into a medical breathing mask, the sensor was able to distinguish between inhalation and exhalation, as well as detecting alcohol consumption.

Odorant molecules, a type of VOC, are added to odorless natural gas to make it detectable by the human nose through interaction with odorant receptors. This allows people to

perceive the presence of gas when it contains these molecules (Fig. 9e). Therefore, detecting odorants plays a vital role in hazardous gas detection, as well as in the food, fragrance, and healthcare industries. An electronic nose (e-nose) integrating catalytic cerium oxide (CeOx) into a LIG array was developed to detect nine different odorant molecules (Fig. 9f).[181] The PI film was spin-coated with cerium nitrate, followed by being directly laser-written to form *in situ* LIG-doped CeO_x nanoparticles. Nine CeLIG gas sensors were fabricated using different laser parameters, and their corresponding responses to the nine scents were analyzed using a machine learning model to extract distinct signal patterns for each target compound (Fig. 9g–i).

Nicotine is a highly addictive organic compound found in tobacco, posing significant health risks through smoking addiction.[182] Excessive nicotine intake can lead to respiratory, cardiovascular, and pulmonary complications. Monitoring nicotine levels is critical in smoking cessation programs, as it enables the assessment of individual smoking behavior and supports personalized interventions to reduce dependency and prevent relapse.[182] A sensor based on LIG fabricated on PI successfully detected nicotine in PBS, achieving a LOD of 4.2183 μM and a highest R^2 of 0.9988 within its linear detection range, using an electrochemical sensing mechanism without functionalizing the working electrode.[182]

Overall, the versatility of LIG in VOC sensing, from its pristine form to its composites with polymers and metal oxides, facilitates the development of flexible sensing platforms while enhancing critical performance metrics. These include improved sensitivity, faster response time, lower LOD, and higher fabrication efficiency, making LIG a promising material for next-generation VOC sensors.

4.4. Integrated, multifunctional sensing platforms

To enable multimodal information acquisition for comprehensive analysis and decision-making, it is essential to combine multiple sensors into a unified platform to simultaneously detect various physical, chemical, and biological signals. Owing to its unique properties, LIG serves as a versatile material that enables high sensitivity, mechanical flexibility, biocompatibility, and scalable production, making it particularly suitable for wearable, implantable, and environmental monitoring applications. In addition to sensors, these multifunctional platforms integrate wireless communication modules, self-powered energy systems, and advanced packaging strategies. These components are essential for enabling seamless data transmission, extended operational autonomy, and enhanced biocompatibility.

Wireless communication modules eliminate the complexity associated with wiring, making them suitable for wearable or implantable devices. These modules also enhance mobility and enable real-time monitoring during movement. For instance, Lin *et al.* integrated a near-field communication (NFC) coil with an inductance of 5 nH and an NFC chip possessing an internal capacitance of 27.5 pF to achieve contactless communication with a smartphone.[183] The AgNP/LIG-based NFC coil, when coupled with a cefazolin-modified LIG electrode, generates an output voltage of 1.5 V, which simultaneously powers a UV LED and enables controlled drug release. This multifunctional platform supports real-time monitoring in combination with programmable drug delivery. To address the needs of vulnerable populations such as the elderly, individuals with disabilities, and infants, Takei *et al.* developed a wearable sensor system that continuously monitors body conditions and provide wireless alarm feedback.[184] A ten-channel signal system, incorporating sensors for tilt, strain, and humidity, allows synchronous acquisition and wireless transmission *via* bluetooth to a user interface. The system includes preprogrammed conditions for independent alarm activation in cases such as prone sleeping, apnea, or excessive humidity in diapers.

For long-term operation, beyond conventional batteries and capacitors, integrating self-powered systems offers a promising approach for developing multifunctional platforms. Among these, triboelectric nanogenerators (TENGs) are frequently employed. Tang *et al.* reported a stretchable and self-powered system composed of a micro-supercapacitor (MSC) array, a wrinkled graphene-based sensor, and a crumpled Au-based TENG.[185] By designing the system to convert human mechanical energy into electrical energy and store it in the MSC array, they enabled self-powered operation of the mechanical sensor. Xu *et al.* also utilized a flexible and stretchable nanogenerator in combination with a planar MSC array to convert biomechanical energy into stable and continuous electrical power.[186] This energy was used to drive wearable sensors that monitor physiological parameters including pulse, strain, temperature, ECG, blood pressure, and blood oxygen levels. The system also included a bluetooth-based wireless transmission module, allowing continuous acquisition of physiological signals in real time. Notably, a perspiration-driven self-powered sensor was developed by Tan *et al.*[187] Using Ni-ZIF-8 modified with lactate oxidase and pyruvate oxidase (Ni-ZIF-8@LOx&POx) on LIG, combined with bilirubin oxidase/LIG and integrated microchannels, the system enabled high-sensitivity and self-powered lactate monitoring in sweat. This approach offers a novel solution for remote healthcare applications.

To enhance user comfort, protect sensitive electronic components, and improve biocompatibility, effective packaging is essential. Research efforts have focused on selecting encapsulating materials that are not only flexible, stretchable, and biocompatible, but also breathable, durable, and chemically inert to ensure long-term stability. Materials such as PDMS and PU are commonly employed due to their softness and compatibility with skin and tissues. In addition, soft encapsulated systems allow the integration of sensing platforms onto irregular surfaces and dynamically moving body parts. Beyond physical protection, encapsulation also serves to prevent moisture ingress, reduce signal noise, and enhance the mechanical resilience of the device under repeated deformation or strain.

LIG-based multifunctional sensing platforms have demonstrated broad applications in health monitoring and disease diagnostics. Among applications, postoperative monitoring and chronic disease management represent critical areas where real-time and continuous health tracking provides substantial

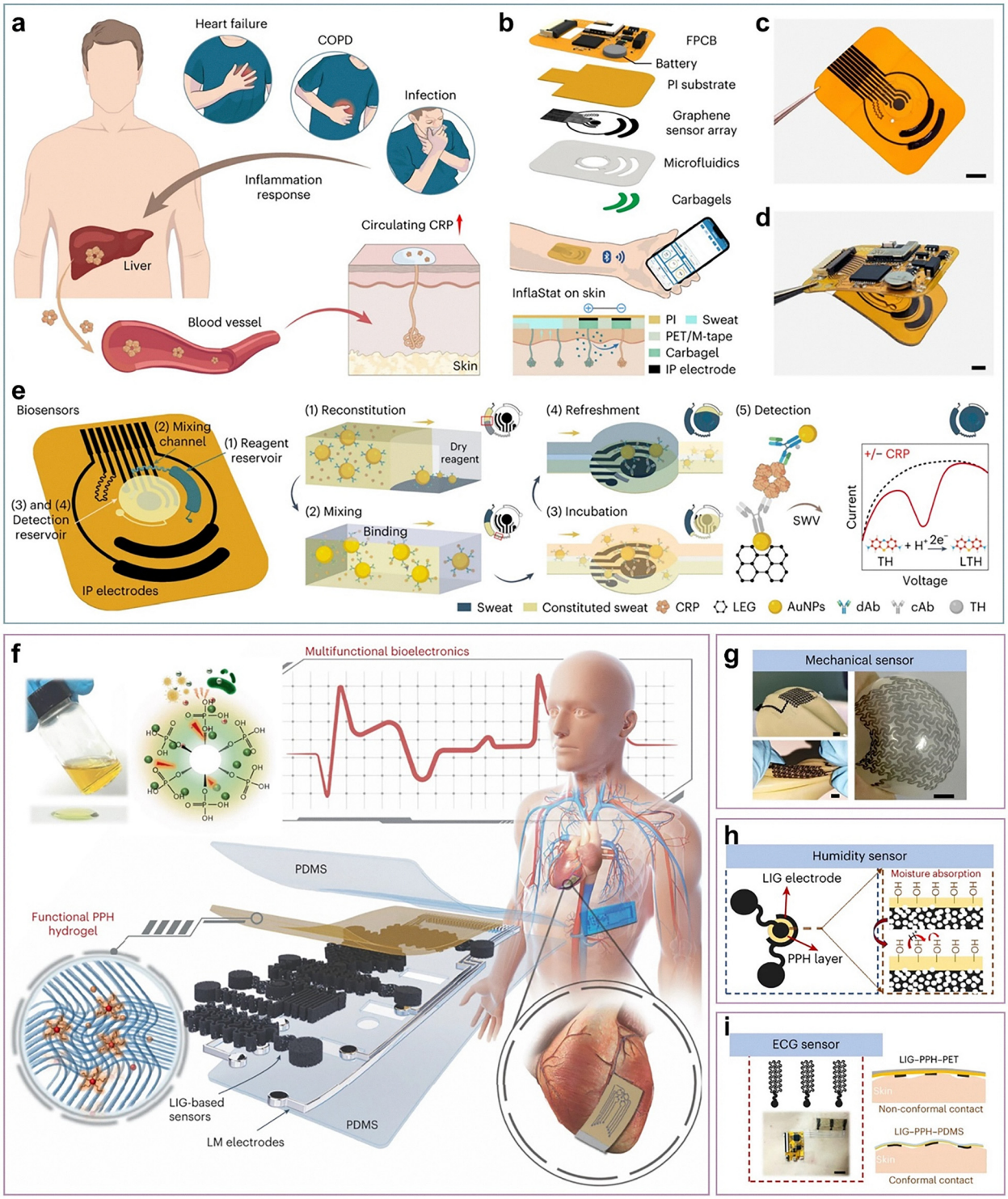

Fig. 10 (a) C-reactive protein (CRP), a biomarker of inflammation, can be secreted through sweat and is linked to various health conditions. (b) Schematic of a skin-interfaced wearable biosensor featuring iontophoresis for sweat extraction, microfluidics for automated sampling and reagent delivery, and a flexible LEG sensor array for multiplexed detection of CRP, pH, temperature, and ionic strength. (c) and (d) Optical images of a disposable microfluidic graphene patch (c) and a fully integrated wireless wearable system (d). Scale bars: 0.5 cm. (e) *In situ* CRP analysis *via* microfluidics with automatic sweat sampling, reagent mixing, and detection. Yellow arrows show fluid flow; red boxes indicate cross-sectional views (1) and (2). Abbreviations: carbagel – carbachol hydrogel; IP – iontophoresis; LTH – leuco-thionine; M-tape – medical tape. Reproduced with permission. Reproduced with permission.[188] Copyright 2023, Springer Nature. (f) Structure of polyvinyl alcohol (PVA)–phytic acid (PA)–honey (PPH) hydrogel-based stretchable nanocomposites with antibacterial and biocompatible properties. (g) LIG–PPH–PDMS film-based sensor on a balloon. Scale bar: 1 cm. (h) Schematic and working principle of a humidity sensor using PPH. (i) Photograph (left) and schematic (right) of an ECG sensor with different substrates on the skin. Scale bar: 2 cm. Reproduced with permission.[16] Copyright 2024, Springer Nature.

clinical value. For instance, in patients with chronic obstructive pulmonary disease, active or past infections, or heart failure, elevated CRP concentrations measured *via* a wearable patch have shown strong correlation with serum levels. Gao *et al.* developed a wearable wireless patch that integrates iontophoresis-based sweat induction, microfluidic channels for sweat sampling and reagent delivery or replacement, and a graphene-based sensor array for the quantitative detection of CRP, ionic strength, pH, and temperature (Fig. 10a–e).[188] These parameters are used for real-time calibration of the CRP sensor. This technology enables dynamic monitoring of CRP levels and provides valuable clinical insights. In principle, the same strategy can be applied to on-demand assessment of other trace-level, disease-related protein biomarkers. In other study, Li *et al.* developed working electrodes for creatinine and lactate sensing using laser-induced backside and frontside transfers, and integrated the system with a robotic arm for precise fabrication.[189] These electrodes were assembled with LIG circuits featuring hydrophilic–hydrophobic interfaces and connected to a custom-designed portable electrochemical workstation that supports open-circuit potential (OCPT) and DPV measurements. This noninvasive sweat sensor could detect potassium ions, creatinine, and lactate, enabling real-time monitoring of kidney function.

To support continuous and noninvasive health assessment in everyday life, Xu *et al.* transferred LIG onto a hydrogel film at low temperature, resulting in a thin, elastic, and conductive nanocomposite (Fig. 10f–i).[190] The hydrogel acts as both an energy dissipation interface and a vertical conductive pathway, introducing continuous deflection cracks into the LIG layer and enhancing its stretchability by over fivefold. This integrated epidermal sensor can simultaneously monitor physical signals such as respiratory rate, skin temperature, humidity, and ECG (Fig. 10g–i). It also enables analysis of signal variations before and after physical activity and detection of angina-related ECG abnormalities in rats. However, several challenges remain for practical use, including improving the breathability of the sensor film and ensuring reliable contact between conformal electronics and the skin.

Besides health monitoring, LIG-based multifunctional platforms also play an important role in human–machine interaction by enabling intuitive and real-time communication between users and electronic systems. Hussain *et al.* developed a fully soft inertial sensor composed of LIG and liquid metal, integrated with sensors for temperature, humidity, and respiration.[191] This multifunctional platform was used to monitor physical activities under various conditions such as standing, walking, jogging, lying down, and getting up. At the interface level, a robotic arm was programmed to perform coordinated operations including movement, rotation, and object manipulation in response to human motion. The printed inertial platform presents strong potential for next-generation wearable motion-tracking systems and soft human–machine interfaces. Human–machine interaction scenarios also include electrooculography and tactile perception systems, machine-learning-assisted dual-function acoustic systems, intelligent speech recognition and motion control platforms, artificial larynx devices, humidity-based non-contact health monitoring systems, and soft, stretchable gesture recognition systems.[17] All of these illustrate the growing versatility of LIG in multifunctional and intelligent wearable electronics for healthcare and interactive technologies.

During the development of multifunctional sensing platforms, a key challenge is developing durable interconnects between rigid circuit modules and flexible LIG-based sensors that remain stable under deformation. Furthermore, LIG-based sensors often encounter cross-sensitivity to stimuli such as pressure, temperature, humidity, strain, pH, and so on. To address this, researchers have explored strategies such as optimizing device architecture, utilizing material-specific properties like the thermoelectric effect, and applying algorithm-assisted signal decoupling. For example, thermoelectric porous LIG has been used to separate strain and temperature signals in self-powered sensors.[192] Despite notable progress, these methods still face limitations, highlighting the need for further innovation to realize reliable and high-performance sensing platforms.

5. Current challenges and future perspectives

LIG has attracted significant attention due to its exceptional properties, low cost, and ease of fabrication, positioning it as a promising material for various applications. Nevertheless, several challenges still impede its widespread adoption and commercialization, primarily related to the fabrication process and precise control over its intrinsic properties.

The first major challenge is achieving consistent properties across different fabrication batches, particularly when LIG is derived from natural materials. For instance, the composition of wood can slightly vary even within different regions of the same tree, significantly influencing the properties of resulting LIG. However, natural materials are essential for sustainability and reducing CO_2 emissions. Therefore, processing natural materials into standardized products with tightly controlled compositions could mitigate variability in LIG properties. In contrast, synthetic polymers offer better control over chemical composition and uniformity, enabling easier LIG formation and facilitating mass production with consistent quality.

Another critical yet often overlooked challenge is ensuring uniformity in the properties and microstructures of differently sized LIG patterns fabricated using identical parameters. LIG formation relies on heat accumulation, meaning fabrication parameters optimized for a specific pattern size may become ineffective when pattern dimensions vary. Thus, different regions within complex patterns exhibit varying properties. We believe deeper research into heat accumulation and parameter optimization according to pattern geometry and dimensions could effectively address this issue.

Additionally, most current LIG electrodes are millimeter or centimeter scale, while micro- or sub-micrometer-scale

electrodes remain relatively unexplored. Smaller-scale electrodes could significantly expand LIG's applicability in microelectronics, brain–machine interfaces, and optoelectronic devices. Advancing nanoscale LIG fabrication using short-wavelength or ultrashort-pulsed lasers, combined with high-precision laser focusing systems, represents a promising direction for future research.

Moreover, despite relatively rapid fabrication compared to conventional graphene patterning methods, the throughput of LIG production remains insufficient for industrial-scale mass production. Enhancing scalability might involve parallel processing methods, such as employing multiple laser scanning heads and integrating roll-to-roll manufacturing techniques to increase productivity.

On the other hand, the potential environmental impacts associated with large-scale production and disposal of LIG biomedical devices need to be comprehensively assessed. We believe that the use of eco-friendly carbon precursors for LIG synthesis plays a crucial role in minimizing environmental impact. Furthermore, the choice of chemicals for LIG functionalization should prioritize environmental safety. It is also essential to assess the composition and potential effects of emissions generated during the LIG fabrication process on both human health and the environment.

Long-term stability presents another challenge for LIG biomedical sensors. LIG can absorb moisture and volatile compounds from its environment,[193,194] potentially affecting its properties and performance over time. Moreover, interactions with biological fluids (*e.g.*, sweat, blood) require comprehensive studies to establish optimal storage conditions, shelf life, and overall durability of sensors in biological environments to ensure their reliability and accuracy.

Furthermore, although preliminary safety studies such as those conducted using zebrafish models have shown encouraging results,[85] extensive investigations into LIG's toxicity and long-term biocompatibility in humans are still necessary. For example, prolonged exposure effects of LIG masks on respiratory organs must be carefully assessed before widespread adoption. Furthermore, the lack of standardized protocols for toxicity, biodegradability, and biocompatibility assessments, along with regulatory uncertainties, hinders the clinical translation and practical application of LIG sensors.

Despite these challenges, LIG holds considerable untapped potential for biomedical applications. Current developments demonstrate the capability of advanced LIG platforms to integrate multiple sensing functionalities, simultaneously monitoring physiological parameters such as body temperature, hydration status, electrophysiological signals, and biomarkers. The continuous collection of multimodal health data enables personalized health monitoring, real-time disease diagnosis, and early prediction of pathological conditions before symptoms appear. Integration with big data analytics, cloud-based data management, and artificial intelligence will significantly advance predictive and personalized healthcare.

Currently, the majority of LIG-based biosensors are designed based on electrochemical transduction mechanisms due to their simplicity, high sensitivity, and ease of operation. Nonetheless, alternative sensing strategies have emerged as promising avenues for further development. Photoelectrochemical biosensors, which integrate light excitation with electrochemical signal generation, offer enhanced sensitivity and reduced background noise due to the spatial separation of excitation and detection processes.[195,196] Moreover, field-effect transistor-based LIG biosensors represent another attractive platform, characterized by their ultra-high sensitivity, miniaturized form factor, and low power requirements.[197]

Commercialization represents another key opportunity for LIG biomedical sensors, as its distinctive advantages over other graphene-like materials make it well-suited for large-scale deployment in next-generation health monitoring technologies. Therefore, LIG biomedical sensors are anticipated to enter commercial markets in the near future, substantially reducing the cost of wearable healthcare devices and increasing accessibility, especially in low-income countries.

Finally, considering Earth's limited resources and the predominantly single-use nature of diagnostic devices, the use of green and widely available materials to fabricate low-cost, eco-friendly, and disposable LIG biomedical sensors offers a strategic advantage for point-of-care diagnostics. This approach holds significant promise to improve healthcare accessibility in resource-limited regions, aligning technological advancements with global sustainability goals.

6. Conclusions

LIG has established itself as an impactful material in the field of biomedical sensing owing to its superior properties, cost effectiveness, and scalable production. These advantages have enabled its integration into a variety of flexible, wearable, and point-of-care devices. Recent advancements have demonstrated the effectiveness of LIG-based sensors in detecting a wide range of physiological, electrophysiological, and biochemical signals relevant to health monitoring and disease diagnostics. Despite promising capabilities, several challenges remain including batch-to-batch variability, limited nanoscale resolution, long-term stability, and the need for standardized biocompatibility and toxicity assessments. Addressing these limitations will be crucial for translating LIG-based technologies into real-world clinical and commercial applications. Looking forward, the successful implementation of LIG in diverse biomedical applications highlights its potential to drive innovation in personalized healthcare. The use of bioderived precursors also aligns with the growing demand for sustainable and eco-friendly electronic materials. As research in this field progresses, LIG is well positioned to contribute significantly to the development of scalable, accessible, and adaptable sensing solutions that address the complex needs of modern medicine and global public health.

Conflicts of interest

The authors declare no conflict of interest.

Data availability

No primary research results, software or code have been included and no new data were generated or analysed as part of this review.

Acknowledgements

This work was supported by the Institute for Health Innovation and Technology (iHealthtech), National University of Singapore (NUS) (seed grant: A-0001415-06-00), the NUS Start-Up Grant (A-0009363-04-00), and the NUSS Professorship Grant (E-468-00-0012-01). Additional support was provided by the Mechanobiology Institute, NUS (grant no. A-8001978-04-00), and the Institute for Functional Intelligent Materials (I-FIM), NUS (grant no. A-0001423-04-00). The authors also acknowledge institutional support from the SIA-NUS Digital Aviation Corp Lab.

References

1 K. I. Bolotin, K. Sikes, Z. Jiang, M. Klima, G. Fudenberg, J. Hone, P. Kim and H. L. Stormer, *Solid State Commun.*, 2008, **146**, 351–355.
2 A. A. Balandin, S. Ghosh, W. Bao, I. Calizo, D. Teweldebrhan, F. Miao and C. N. Lau, *Nano Lett.*, 2008, **8**, 902–907.
3 A. Zandiatashbar, G.-H. Lee, S. J. An, S. Lee, N. Mathew, M. Terrones, T. Hayashi, C. R. Picu, J. Hone and N. Koratkar, *Nat. Commun.*, 2014, **5**, 3186.
4 M. D. Stoller, S. Park, Y. Zhu, J. An and R. S. Ruoff, *Nano Lett.*, 2008, **8**, 3498–3502.
5 K. S. Novoselov, L. Colombo, P. Gellert, M. Schwab and K. Kim, *Nature*, 2012, **490**, 192–200.
6 J. Lin, Z. Peng, Y. Liu, F. Ruiz-Zepeda, R. Ye, E. L. Samuel, M. J. Yacaman, B. I. Yakobson and J. M. Tour, *Nat. Commun.*, 2014, **5**, 5714.
7 A. Lamberti, M. Serrapede, G. Ferraro, M. Fontana, F. Perrucci, S. Bianco, A. Chiolerio and S. Bocchini, *2D Mater.*, 2017, **4**, 035012.
8 T. S. D. Le, Y. A. Lee, H. K. Nam, K. Y. Jang, D. Yang, B. Kim, K. Yim, S. W. Kim, H. Yoon and Y. J. Kim, *Adv. Funct. Mater.*, 2022, **32**, 2107768.
9 T. S. D. Le, S. Park, J. An, P. S. Lee and Y. J. Kim, *Adv. Funct. Mater.*, 2019, **29**, 1902771.
10 Y. Chyan, R. Ye, Y. Li, S. P. Singh, C. J. Arnusch and J. M. Tour, *ACS Nano*, 2018, **12**, 2176–2183.
11 J. Sha, Y. Li, R. Villegas Salvatierra, T. Wang, P. Dong, Y. Ji, S.-K. Lee, C. Zhang, J. Zhang and R. H. Smith, *ACS Nano*, 2017, **11**, 6860–6867.
12 X. Zang, C. Jian, S. Ingersoll, H. Li, J. Adams, Z. Lu, N. Ferralis and J. Grossman, *Sci. Adv.*, 2020, **6**, eaaz5231.
13 A. Vashisth, M. Kowalik, J. C. Gerringer, C. Ashraf, A. C. Van Duin and M. J. Green, *ACS Appl. Nano Mater.*, 2020, **3**, 1881–1890.
14 Y. Chen, J. Long, S. Zhou, D. Shi, Y. Huang, X. Chen, J. Gao, N. Zhao and C. P. Wong, *Small Methods*, 2019, **3**, 1900208.
15 R. Ye, Y. Chyan, J. Zhang, Y. Li, X. Han, C. Kittrell and J. M. Tour, *Adv. Mater.*, 2017, **29**, 1702211.
16 Y. Lu, G. Yang, S. Wang, Y. Zhang, Y. Jian, L. He, T. Yu, H. Luo, D. Kong and Y. Xianyu, *Nat. Electron.*, 2024, **7**, 51–65.
17 T. Raza, M. K. Tufail, A. Ali, A. Boakye, X. Qi, Y. Ma, A. Ali, L. Qu and M. Tian, *ACS Appl. Mater. Interfaces*, 2022, **14**, 54170–54181.
18 S. Yang, B. Zheng, H. Qian, Q. Yan, G. Huang, J. Lin and C. Wan, *ACS Appl. Nano Mater.*, 2024, **7**, 25241–25248.
19 A. Dallinger, K. Keller, H. Fitzek and F. Greco, *ACS Appl. Mater. Interfaces*, 2020, **12**, 19855–19865.
20 A. Kaidarova, N. Alsharif, B. N. M. Oliveira, M. Marengo, N. R. Geraldi, C. M. Duarte and J. Kosel, *Global Challenges*, 2020, **4**, 2000001.
21 B. Sun, R. N. McCay, S. Goswami, Y. Xu, C. Zhang, Y. Ling, J. Lin and Z. Yan, *Adv. Mater.*, 2018, **30**, 1804327.
22 J. Sun, Z. Huang, X. Zhang, H. Xiong, W. Yu, S. Mou, W. Zhu and H. Wan, *Chemosensors*, 2024, **13**, 3.
23 L. Yang, H. Ji, C. Meng, Y. Li, G. Zheng, X. Chen, G. Niu, J. Yan, Y. Xue, S. Guo and H. Cheng, *ACS Appl. Mater. Interfaces*, 2022, **14**, 17818–17825.
24 L. Yang, G. Zheng, Y. Cao, C. Meng, Y. Li, H. Ji, X. Chen, G. Niu, J. Yan, Y. Xue and H. Cheng, *Microsyst. Nanoeng.*, 2022, **8**, 78.
25 J. Guo, M. Zhao, C. Chen, F. Wang and Z. Chen, *Analyst*, 2023, **149**, 137–147.
26 R. M. Torrente-Rodriguez, H. Lukas, J. Tu, J. Min, Y. Yang, C. Xu, H. B. Rossiter and W. Gao, *Matter*, 2020, **3**, 1981–1998.
27 H. Hamidi, R. Murray, V. Vezzoni, S. Bozorgzadeh, A. O'Riordan, D. Pontiroli, M. Riccò, A. J. Quinn and D. Iacopino, *Biosens. Bioelectron.:X*, 2025, **24**, 100600.
28 J. Ion, *Laser processing of engineering materials: principles, procedure and industrial application*, Elsevier, 2005.
29 T. S. D. Le, S. Park, J. An, P. S. Lee and Y. J. Kim, *Adv. Funct. Mater.*, 2019, **29**, 1902771.
30 K. Khorkov, D. Kochuev, V. Ilin, R. Chkalov, V. Prokoshev and S. Arakelian, *J. Phys.:Conf. Ser.*, 2018, **951**, 012014.
31 Y. Miyamoto, H. Zhang and D. Tománek, *Phys. Rev. Lett.*, 2010, **104**, 208302.
32 Y. Dong, S. C. Rismiller and J. Lin, *Carbon*, 2016, **104**, 47–55.
33 D. B. Schüpfer, F. Badaczewski, J. Peilstöcker, J. M. Guerra-Castro, H. Shim, S. Firoozabadi, A. Beyer, K. Volz, V. Presser and C. Heiliger, *Carbon*, 2021, **172**, 214–227.
34 J. Gaudin, O. Peyrusse, J. Chalupský, M. Toufarová, L. Vyšín, V. Hájková, R. Sobierajski, T. Burian, S. Dastjani-Farahani and A. Graf, *Phys. Rev. B:Condens. Matter Mater. Phys.*, 2012, **86**, 024103.
35 A. F. Carvalho, A. J. Fernandes, C. Leitão, J. Deuermeier, A. C. Marques, R. Martins, E. Fortunato and F. M. Costa, *Adv. Funct. Mater.*, 2018, **28**, 1805271.
36 M. G. Stanford, C. Zhang, J. D. Fowlkes, A. Hoffman, I. N. Ivanov, P. D. Rack and J. M. Tour, *ACS Appl. Mater. Interfaces*, 2020, **12**, 10902–10907.

37 E. Abbe, *Arch. Mikrosk. Anat.*, 1873, **9**, 413–468.
38 E. H. Stelzer, *Nature*, 2002, **417**, 806–807.
39 L. X. Duy, Z. Peng, Y. Li, J. Zhang, Y. Ji and J. M. Tour, *Carbon*, 2018, **126**, 472–479.
40 S. Hong, J. Kim, S. Jung, J. Lee and B. S. Shin, *ACS Mater. Lett.*, 2023, **5**, 1261–1270.
41 H. Sun, *A practical guide to handling laser diode beams*, Springer, 2015.
42 Z. Zhang, M. Song, J. Hao, K. Wu, C. Li and C. Hu, *Carbon*, 2018, **127**, 287–296.
43 C. Kim, E. Hwang, J. Kwon, T. H. Jang, W. C. Lee, S. H. Kim, J. Park, M. T. Lee, H. Kim and S. Hong, *Adv. Sci.*, 2023, **10**, 2301208.
44 Y. Jung, J. Min, J. Choi, J. Bang, S. Jeong, K. R. Pyun, J. Ahn, Y. Cho, S. Hong and S. Hong, *Appl. Mater. Today*, 2022, **29**, 101589.
45 T. Xing, Y. Huang, K. Zhang and J. Wu, *RSC Adv.*, 2014, **4**, 53628–53633.
46 L. Lu, D. Zhang, Y. Xie and W. Wang, *J. Energy Storage*, 2022, **51**, 104458.
47 T.-S. D. Le, D. Yang, H. K. Nam, Y. Lee, C. T. Lim, B. J. Lee, S.-W. Kim and Y.-J. Kim, *ACS Nano*, 2024, **18**, 33220–33231.
48 J. Lim, S. Park, H. Cho, Y. Lee, I. Ha, Y. Kim, E. Hwang, H. Lee, J. Shin and J. Kwon, *Chem. Eng. J.*, 2022, **428**, 131050.
49 J. Zhang, R. Xu, J. Feng, Y. Xie and T. Zhou, *Ind. Eng. Chem. Res.*, 2021, **60**, 11161–11170.
50 R. R. Gattass and E. Mazur, *Nat. Photonics*, 2008, **2**, 219–225.
51 K. Sugioka and Y. Cheng, *Light:Sci. Appl.*, 2014, **3**, e149–e149.
52 F. Morosawa, S. Hayashi and M. Terakawa, *ACS Sustainable Chem. Eng.*, 2021, **9**, 2955–2961.
53 M. Hu, J. Jj Nivas, M. Valadan, R. Fittipaldi, A. Vecchione, R. Bruzzese, C. Altucci and S. Amoruso, *Appl. Surf. Sci.*, 2022, **606**, 154869.
54 R. Ye, X. Han, D. V. Kosynkin, Y. Li, C. Zhang, B. Jiang, A. A. Martí and J. M. Tour, *ACS Nano*, 2018, **12**, 1083–1088.
55 D. Yang, H. K. Nam, T.-S. D. Le, J. Yeo, Y. Lee, Y.-R. Kim, S.-W. Kim, H.-J. Choi, H. C. Shim and S. Ryu, *ACS Nano*, 2023, **17**, 18893–18904.
56 Y. Zhu, H. Cai, H. Ding, N. Pan and X. Wang, *ACS Appl. Mater. Interfaces*, 2019, **11**, 6195–6200.
57 S. P. Singh, Y. Li, J. Zhang, J. M. Tour and C. J. Arnusch, *ACS Nano*, 2018, **12**, 289–297.
58 J. Liu, L. Zhang, C. Yang and S. Tao, *J. Mater. Chem. A*, 2019, **7**, 21168–21175.
59 X. Li, W. Cai, L. Colombo and R. S. Ruoff, *Nano Lett.*, 2009, **9**, 4268–4272.
60 R. Trusovas, K. Ratautas, G. Račiukaitis and G. Niaura, *Appl. Surf. Sci.*, 2019, **471**, 154–161.
61 Y. Li, D. X. Luong, J. Zhang, Y. R. Tarkunde, C. Kittrell, F. Sargunaraj, Y. Ji, C. J. Arnusch and J. M. Tour, *Adv. Mater.*, 2017, **29**, 1700496.
62 A. Lamberti, F. Clerici, M. Fontana and L. Scaltrito, *Adv. Energy Mater.*, 2016, **6**, 1600050.
63 Y.-J. Kim, T.-S. D. Le, H. K. Nam, D. Yang and B. Kim, *CIRP Ann.*, 2021, **70**, 443–446.
64 C. Zhang, C. Zhang, X. Wu, J. Ping and Y. Ying, *npj Flexible Electron.*, 2022, **6**, 43.
65 A. K. Thakur, S. P. Singh, M. N. Kleinberg, A. Gupta and C. J. Arnusch, *ACS Appl. Mater. Interfaces*, 2019, **11**, 10914–10921.
66 T. Pinheiro, R. Correia, M. Morais, J. Coelho, E. Fortunato, M. G. F. Sales, A. C. Marques and R. Martins, *ACS Nano*, 2022, **16**, 20633–20646.
67 J. Xu, X. Li, H. Chang, B. Zhao, X. Tan, Y. Yang, H. Tian, S. Zhang and T.-L. Ren, *ACS Nano*, 2022, **16**, 6687–6699.
68 D. X. Luong, K. Yang, J. Yoon, S. P. Singh, T. Wang, C. J. Arnusch and J. M. Tour, *ACS Nano*, 2019, **13**, 2579–2586.
69 T. S. D. Le, H. P. Phan, S. Kwon, S. Park, Y. Jung, J. Min, B. J. Chun, H. Yoon, S. H. Ko and S. W. Kim, *Adv. Funct. Mater.*, 2022, **32**, 2205158.
70 D. Yang, H. K. Nam, Y. Lee, S. Kwon, J. Lee, H. Yoon and Y. J. Kim, *Adv. Funct. Mater.*, 2025, **35**, 2411257.
71 R. J. Moon, A. Martini, J. Nairn, J. Simonsen and J. Youngblood, *Chem. Soc. Rev.*, 2011, **40**, 3941–3994.
72 Y. Wang, G. Wang, M. He, F. Liu, M. Han, T. Tang and S. Luo, *Small*, 2021, **17**, 2103322.
73 J. Nasser, J. Lin, L. Zhang and H. A. Sodano, *Carbon*, 2020, **162**, 570–578.
74 X. Han, R. Ye, Y. Chyan, T. Wang, C. Zhang, L. Shi, T. Zhang, Y. Zhao and J. M. Tour, *ACS Appl. Nano Mater.*, 2018, **1**, 5053–5061.
75 L. Cheng, C. S. Yeung, L. Huang, G. Ye, J. Yan, W. Li, C. Yiu, F.-R. Chen, H. Shen and B. Z. Tang, *Nat. Commun.*, 2024, **15**, 2925.
76 R. S. Raman, A. Sanjid, P. C. Banerjee, A. K. Arya, R. Parmar, M. Amati and L. Gregoratti, *Small*, 2024, **20**, 2302498.
77 S. Suzuki and M. Yoshimura, *Sci. Rep.*, 2017, **7**, 14851.
78 Y. Liu, Y. Ma, J. Yang, S. Zhang, N. Wu, P. Wang and L. Wang, *Chem. Eng. J.*, 2025, **508**, 160721.
79 S. P. Lee, P. S. Chee, C. H. Tan, K. F. Chong, E. H. Lim and C. Guan, *Chem. Eng. J.*, 2024, 156110.
80 I. I. Kulakova and G. V. Lisichkin, *Moscow Univ. Chem. Bull.*, 2022, **77**, 307–321.
81 C. Fenzl, P. Nayak, T. Hirsch, O. S. Wolfbeis, H. N. Alshareef and A. J. Baeumner, *ACS Sens.*, 2017, **2**, 616–620.
82 Y. Chong, Y. Ma, H. Shen, X. Tu, X. Zhou, J. Xu, J. Dai, S. Fan and Z. Zhang, *Biomaterials*, 2014, **35**, 5041–5048.
83 O. Akhavan, E. Ghaderi and A. Akhavan, *Biomaterials*, 2012, **33**, 8017–8025.
84 O. Akhavan, E. Ghaderi, H. Emamy and F. Akhavan, *Carbon*, 2013, **54**, 419–431.
85 M. d'Amora, A. Lamberti, M. Fontana and S. Giordani, *J. Phys. Mater.*, 2020, **3**, 034008.
86 R. Park, D. H. Lee, C. S. Koh, Y. W. Kwon, S. Y. Chae, C. S. Kim, H. H. Jung, J. Jeong and S. W. Hong, *Adv. Healthcare Mater.*, 2024, **13**, 2301753.

87 W. Wang, B. Han, Y. Zhang, Q. Li, Y. L. Zhang, D. D. Han and H. B. Sun, *Adv. Funct. Mater.*, 2021, **31**, 2006179.
88 M. G. Stanford, J. T. Li, Y. Chen, E. A. McHugh, A. Liopo, H. Xiao and J. M. Tour, *ACS Nano*, 2019, **13**, 11912–11920.
89 L. Huang, S. Xu, Z. Wang, K. Xue, J. Su, Y. Song, S. Chen, C. Zhu, B. Z. Tang and R. Ye, *ACS Nano*, 2020, **14**, 12045–12053.
90 M. Gu, L. Huang, Z. Wang, W. Guo, L. Cheng, Y. Yuan, Z. Zhou, L. Hu, S. Chen, C. Shen, B. Z. Tang and R. Ye, *Small*, 2021, **17**, e2102841.
91 S. Beikzadeh, A. Akbarinejad, J. Taylor, S. Swift, D. Simonov, J. Ross, J. Perera, P. A. Kilmartin and J. Travas-Sejdic, *Appl. Mater. Today*, 2023, **31**, 101753.
92 M. Singh, C. Zannella, V. Folliero, R. Di Girolamo, F. Bajardi, A. Chianese, L. Altucci, A. Damasco, M. R. Del Sorbo, C. Imperatore, M. Rossi, M. Valadan, M. Varra, A. Vergara, G. Franci, M. Galdiero and C. Altucci, *Front. Bioeng. Biotechnol.*, 2020, **8**, 569967.
93 X. Huang, H. Li, J. Li, L. Huang, K. Yao, C. K. Yiu, Y. Liu, T. H. Wong, D. Li, M. Wu, Y. Huang, Z. Gao, J. Zhou, Y. Gao, J. Li, Y. Jiao, R. Shi, B. Zhang, B. Hu, Q. Guo, E. Song, R. Ye and X. Yu, *Nano Lett.*, 2022, **22**, 3447–3456.
94 J. Kaur, K. Swetha, M. Singh, A. Abduvakhidov, M. Varra, M. Lakavathu, J. Adam, A. Prajapati, S. R. Bonam, C. Altucci and R. Kurapati, *Nanoscale*, 2025, **17**, 11293–11304.
95 W. P. Cheshire Jr, *Auton. Neurosci.*, 2016, **196**, 91–104.
96 M. Umar, F. S. Irani, S. S. Mirbakht and M. K. Yapici, *Adv. Electron. Mater.*, 2024, **10**, 2300723.
97 M. Marengo, G. Marinaro and J. Kosel, *IEEE Sens.*, 2017, 1–3.
98 A. Di Bartolomeo, M. Sarno, F. Giubileo, C. Altavilla, L. Iemmo, S. Piano, F. Bobba, M. Longobardi, A. Scarfato and D. Sannino, *J. Appl. Phys.*, 2009, **105**, 064518.
99 P. Sahatiya, S. K. Puttapati, V. V. Srikanth and S. Badhulika, *Flexible Printed Electron.*, 2016, **1**, 025006.
100 D. Yoon, Y.-W. Son and H. Cheong, *Nano Lett.*, 2011, **11**, 3227–3231.
101 A. Müller, M. C. Wapler and U. Wallrabe, *Soft Matter*, 2019, **15**, 779–784.
102 S. Luo, P. T. Hoang and T. Liu, *Carbon*, 2016, **96**, 522–531.
103 H. Wang, Z. Zhao, P. Liu and X. Guo, *npj Flexible Electron.*, 2022, **6**, 26.
104 T. Raza, M. K. Tufail, A. Ali, A. Boakye, X. Qi, Y. Ma, A. Ali, L. Qu and M. Tian, *ACS Appl. Mater. Interfaces*, 2022, **14**, 54170–54181.
105 A. M. Barja, Y. K. Ryu, S. Tarancón, E. Tejado, A. Hamada, A. Velasco and J. Martinez, *ACS Omega*, 2024, **9**, 38359–38370.
106 S. Yang, Y. Ling, Q. Wu, H. Zhang, Z. Yan, G. Huang, J. Lin and C. Wan, *J. Mater. Chem. C*, 2022, **10**, 11730–11738.
107 L.-Q. Tao, H. Tian, Y. Liu, Z.-Y. Ju, Y. Pang, Y.-Q. Chen, D.-Y. Wang, X.-G. Tian, J.-C. Yan and N.-Q. Deng, *Nat. Commun.*, 2017, **8**, 14579.
108 H. Wang, H. Wang, Y. Wang, X. Su, C. Wang, M. Zhang, M. Jian, K. Xia, X. Liang and H. Lu, *ACS Nano*, 2020, **14**, 3219–3226.
109 Y.-K. Shin, K.-H. Kim and M.-H. Seo, *Micro Nano Syst. Lett.*, 2023, **11**, 9.
110 Y. Li, Z. Yang, X. Chen, S. Zhang, S. Xu, P. Li, L. Yi and F. Liu, *ACS Appl. Electron. Mater.*, 2024, **6**, 5117–5125.
111 N. V. Thakor and Y.-S. Zhu, *IEEE Trans. Biomed. Eng.*, 1991, **38**, 785–794.
112 W. Klimesch, *Brain Res. Rev.*, 1999, **29**, 169–195.
113 B. Xu, A. Akhtar, Y. Liu, H. Chen, W.-H. Yeo, S. Park, B. Boyce, H. Kim, J. Yu and H.-Y. Lai, *Adv. Mater.*, 2015, **28**, 4462.
114 H. Wu, G. Yang, K. Zhu, S. Liu, W. Guo, Z. Jiang and Z. Li, *Adv. Sci.*, 2021, **8**, 2001938.
115 A. Miyamoto, S. Lee, N. F. Cooray, S. Lee, M. Mori, N. Matsuhisa, H. Jin, L. Yoda, T. Yokota and A. Itoh, *Nat. Nanotechnol.*, 2017, **12**, 907–913.
116 Q. Zhang, M. Qu, X. Liu, Y. Cui, H. Hu, Q. Li, M. Jin, J. Xian, Z. Nie and C. Zhang, *Adv. Mater. Interfaces*, 2023, **10**, 2201735.
117 J. Liao, X. Zhang, Z. Sun, H. Chen, J. Fu, H. Si, C. Ge and S. Lin, *Biosensors*, 2022, **12**, 397.
118 R. G. Hjort, R. R. A. Soares, J. Li, D. Jing, L. Hartfiel, B. Chen, B. Van Belle, M. Soupir, E. Smith, E. McLamore, J. C. Claussen and C. L. Gomes, *Mikrochim. Acta*, 2022, **189**, 122.
119 R. R. A. Soares, R. G. Hjort, C. C. Pola, D. Jing, V. S. Cecon, J. C. Claussen and C. L. Gomes, *Mikrochim. Acta*, 2023, **190**, 43.
120 I. Diédhiou, A. Raouafi, S. Hamzaoui, M. Fall and N. Raouafi, *Sens. Diagn.*, 2025, **4**, 202–215.
121 V. Reyes-Loaiza, J. De La Roche, E. Hernandez-Renjifo, O. Idarraga, M. Da Silva, D. P. Valencia, T. Ghneim-Herrera and A. Jaramillo-Botero, *Sci. Rep.*, 2024, **14**, 5772.
122 H. Ali, D. Gupta, R. Gupta and N. Verma, *Chem. Eng. Process.*, 2022, **181**, 109146.
123 P. S. Tan, E. Vaughan, J. Islam, N. Burke, D. Iacopino and J. B. Tierney, *Nanomaterials*, 2021, **11**, 2110.
124 D. Ghosh, R. Tabassum, P. P. Sarkar, M. D. A. Rahman, A. H. Jalal, N. Islam and A. Ashraf, *ACS Appl. Bio Mater.*, 2024, **7**, 3143–3153.
125 R. Tabassum, P. P. Sarkar, A. H. Jalal, A. Ashraf and N. Islam, *Polymers*, 2024, **16**, 2069.
126 T. A. Matias, R. G. Rocha, L. V. Faria, E. M. Richter and R. A. A. Munoz, *ChemElectroChem*, 2022, **9**, e202200339.
127 E. Vaughan, C. Santillo, M. Setti, C. Larrigy, A. J. Quinn, G. Gentile, M. Lavorgna and D. Iacopino, *Adv. Sens. Res.*, 2023, **2**, 2300026.
128 M. Shinde and G. Slaughter, *Front. Lab Chip Technol.*, 2025, **4**, 1549365.
129 S. Choudhury, S. Zafar, D. Deepak, A. Panghal, B. Lochab and S. S. Roy, *J. Mater. Chem. B*, 2024, **13**, 274–287.
130 X. Hui, X. Xuan, J. Kim and J. Y. Park, *Electrochim. Acta*, 2019, **328**, 135066.
131 T. Beduk, J. I. de Oliveira Filho, A. Ait Lahcen, V. Mani and K. N. Salama, *Langmuir*, 2021, **37**, 13890–13902.
132 G. Bhattacharya, S. J. Fishlock, S. Hussain, S. Choudhury, A. Xiang, B. Kandola, A. Pritam, N. Soin, S. S. Roy and

J. A. McLaughlin, *ACS Appl. Mater. Interfaces*, 2022, **14**, 31109–31120.
133 R. Gupta, T. Santra, S. K. Misra and N. Verma, *Microchem. J.*, 2024, **207**, 111895.
134 S. Rauf, V. Mani, A. A. Lahcen, S. Yuvaraja, T. Beduk and K. N. Salama, *Electrochim. Acta*, 2021, **386**, 138489.
135 A. K. Thakur, P. Sengodu, A. H. Jadhav and M. Malmali, *ACS Omega*, 2024, **9**, 7869–7880.
136 S. H. Park and J. J. Pak, *Sensors*, 2024, **24**, 6945.
137 Z. Zhang, L. Huang, Y. Chen, Z. Qiu, X. Meng and Y. Li, *RSC Adv.*, 2024, **14**, 1034–1050.
138 P. Preechakasedkit, C. Pulsrikarn, S. Nuanualsuwan, N. Rattanadilok Na Phuket, D. Citterio and N. Ruecha, *Anal. Chem.*, 2024, **96**, 15476–15483.
139 R. R. A. Soares, R. G. Hjort, C. C. Pola, K. Parate, E. L. Reis, N. F. F. Soares, E. S. McLamore, J. C. Claussen and C. L. Gomes, *ACS Sens.*, 2020, **5**, 1900–1911.
140 L. Sembranti, A. Bonini, F. Vivaldi, N. Poma, D. Biagini, A. Dallinger, F. Greco, A. Tavanti and F. Di Francesco, *Talanta*, 2025, **282**, 127014.
141 K. Zhou, V. Kammarchedu, D. Butler, P. Soltan Khamsi and A. Ebrahimi, *Adv. Healthcare Mater.*, 2022, **11**, e2200773.
142 G. Moreira, H. Qian, S. P. A. Datta, N. Bliznyuk, J. Carpenter, D. Dean, E. McLamore and D. Vanegas, *PLoS One*, 2023, **18**, e0290256.
143 Y. Zhou, W. Chen, G. Wang, Z. Lei, M. Zhang and Y. Li, *Anal. Methods*, 2024, **16**, 5069–5081.
144 S. Inlumphan, W. Wongwiriyapan, N. Khemasiri, P. Rattanawarinchai, P. Leepheng, P. Luengrojanakul, T. Wuttikhun, M. Obata, M. Fujishige, K. Takeuchi, M. P. Reilly, T. Uwanno, M. Horprathum, S. Porntheeraphat, K. Sitthisuwannakul, S. Phanthanawiboon and A. Klamchuen, *Sens. Actuators Rep.*, 2025, **9**, 100276.
145 Z. Li, L. Huang, L. Cheng, W. Guo and R. Ye, *Small Methods*, 2024, **8**, e2400118.
146 S. Aftab, G. Koyyada, M. Mukhtar, F. Kabir, G. Nazir, S. A. Memon, M. Aslam, M. A. Assiri and J. H. Kim, *ACS Sens.*, 2024, **9**, 4536–4554.
147 F. Zheng, H.-Y. Jiang, X.-T. Yang, J.-H. Guo, L. Sun, Y.-Y. Guo, H. Xu and M.-S. Yao, *Chem. Eng. J.*, 2024, **490**, 151874.
148 X. Tang, A. Du and L. Kou, *Comput. Mol. Sci.*, 2018, **8**, e1361.
149 Z. Yin, Y. Yang, C. Hu, J. Li, B. Qin and X. Yang, *NPG Asia Mater.*, 2024, **16**, 8.
150 M. G. Stanford, K. Yang, Y. Chyan, C. Kittrell and J. M. Tour, *ACS Nano*, 2019, **13**, 3474–3482.
151 J. Zhu, X. Huang and W. Song, *ACS Nano*, 2021, **15**, 18708–18741.
152 A. Turlybekuly, Y. Shynybekov, B. Soltabayev, G. Yergaliuly and A. Mentbayeva, *ACS Sens.*, 2024, **9**, 6358–6371.
153 M. Maniscalco, S. Fuschillo, I. Mormile, A. Detoraki, G. Sarnelli, A. Paulis, G. Spadaro, E. Cantone and F. Path-2 Task, *Cells*, 2023, **12**, 2518.
154 B. Buszewski, M. Kesy, T. Ligor and A. Amann, *Biomed. Chromatogr.*, 2007, **21**, 553–566.
155 M. P. van der Schee, T. Paff, P. Brinkman, W. M. C. van Aalderen, E. G. Haarman and P. J. Sterk, *Chest*, 2015, **147**, 224–231.
156 M. Nuijsink, W. C. J. Hop, J. C. D. Jongste, P. J. Sterk and A. E. J. Duiverman, *J. Asthma*, 2013, **50**, 560–564.
157 J. Zhao, N. Yi, X. Ding, S. Liu, J. Zhu, A. C. Castonguay, Y. Gao, L. D. Zarzar and H. Cheng, *Chem. Eng. J.*, 2023, **456**, 140956.
158 J. Zhu, M. Cho, Y. Li, I. Cho, J. H. Suh, D. D. Orbe, Y. Jeong, T. L. Ren and I. Park, *ACS Appl. Mater. Interfaces*, 2019, **11**, 24386–24394.
159 M. Lim, J. Y. Kim, H. Kang, T. W. Yun, H.-B. Cho and Y.-H. Choa, *Sens. Actuators Rep.*, 2024, **8**, 100247.
160 H. Rhyu, S. Lee, M. Kang, D. Yoon, S. Myung, W. Song, S. S. Lee and J. Lim, *RSC Adv.*, 2023, **13**, 13128–13133.
161 H. Cheng, S. Huang, Z. Xing, L. Yang, J. Yu and Y. Zhong, *Front. Phys.*, 2024, **12**, 1446416.
162 G. Qian, Q. Peng, H. Wang, S. Wang and W. Dai, *Front. Mater.*, 2020, **7**, 580245.
163 W. Yan, W. Yan, T. Chen, J. Xu, Q. Tian and D. Ho, *ACS Appl. Nano Mater.*, 2020, **3**, 2545–2553.
164 N. Yi, Z. Cheng, H. Li, L. Yang, J. Zhu, X. Zheng, Y. Chen, Z. Liu, H. Zhu and H. Cheng, *Mater. Today Phys.*, 2020, **15**, 100265.
165 C. Zhang, J. Chen, J. Gao, G. Tan, S. Bai, K. Weng, H. M. Chen, X. Ding, H. Cheng, Y. Yang and J. Wang, *Nano Lett.*, 2023, **23**, 3435–3443.
166 H. Lim, H. Kwon, H. Kang, J. E. Jang and H. J. Kwon, *Nat. Commun.*, 2023, **14**, 3114.
167 A. Abbaszadeh, S. Makouei and S. Meshgini, *Photonic Nanostruct.*, 2021, **44**, 100917.
168 D. Wu, Q. Peng, S. Wu, G. Wang, L. Deng, H. Tai, L. Wang, Y. Yang, L. Dong, Y. Zhao, J. Zhao, D. Sun and L. Lin, *Sensors*, 2018, **18**, 4405.
169 J. C. Santos-Ceballos, F. Salehnia, A. Romero, X. Vilanova and E. Llobet, *IEEE Sens. J.*, 2024, **24**, 9366–9374.
170 X. Duan, Z. Duan, Y. Zhang, B. Liu, X. Li, Q. Zhao, Z. Yuan, Y. Jiang and H. Tai, *Sens. Actuators, B*, 2022, **369**, 132302.
171 J. Wen, S. Wang, J. Feng, J. Ma, H. Zhang, P. Wu, G. Li, Z. Wu, F. Meng, L. Li and Y. Tian, *J. Mater. Chem.*, 2024, **12**, 6190–6210.
172 J. C. Santos-Ceballos, F. Salehnia, F. Guell, A. Romero, X. Vilanova and E. Llobet, *Sensors*, 2024, **24**, 7832.
173 Z. Li, H. Li, M. K. LaGasse and K. S. Suslick, *Anal. Chem.*, 2016, **88**, 5615–5620.
174 R. Jalandra, G. B. V. S. Lakshmi, T. K. Dhiman, M. Sharma, A. Kumar and P. R. Solanki, *J. Electrochem. Soc.*, 2023, **170**, 027504.
175 K. Kalantar-Zadeh, K. J. Berean, R. E. Burgell, J. G. Muir and P. R. Gibson, *Nat. Rev. Gastroenterol. Hepatol.*, 2019, **16**, 733–747.
176 E. Mutuyemungu, M. Singh, S. Liu and D. J. Rose, *J. Funct. Foods*, 2023, **100**, 105367.
177 M. Dosi, I. Lau, Y. Zhuang, D. S. A. Simakov, M. W. Fowler and M. A. Pope, *ACS Appl. Mater. Interfaces*, 2019, **11**, 6166–6173.

178 K. K. Adhikari, L. Ali, J. Wei, Y. Yi, X. Tang, Z. Li, J. Gao, L. Mei, Y. Qu, J. Yin and C. Wang, *Chem. Eng. J.*, 2024, **499**, 155984.
179 R. Murray, A. Muriqi, C. Larrigy, A. Russo, M. T. Mengistu, D. Iacopino, C. Fitzpatrick, M. Nolan and A. J. Quinn, *ACS Sustainable Chem. Eng.*, 2024, **12**, 15063–15076.
180 D. Li, Y. Shao, Q. Zhang, M. Qu, J. Ping, Y. Fu and J. Xie, *Analyst*, 2021, **146**, 5704–5713.
181 H. Lim, H. Kwon, J. E. Jang and H. J. Kwon, *ACS Nano*, 2025, **19**, 17850–17862.
182 B. N. Badrol Hisham, R. A. Rahim, A. N. Nordin, A. A. Md Ralib, N. F. Za'bah, L. H. Tung and Z. Mohd Zain, *IIUM Eng. J.*, 2025, **26**, 293–307.
183 J. Zhu, Y. Xiao, X. Zhang, Y. Tong, J. Li, K. Meng, Y. Zhang, J. Li, C. Xing, S. Zhang, B. Bao, H. Yang, M. Gao, T. Pan, S. Liu, F. Lorestani, H. Cheng and Y. Lin, *Adv. Mater.*, 2024, **36**, e2400236.
184 K. Xu, Y. Fujita, Y. Lu, S. Honda, M. Shiomi, T. Arie, S. Akita and K. Takei, *Adv. Mater.*, 2021, **33**, e2008701.
185 C. Zhang, Z. Peng, C. Huang, B. Zhang, C. Xing, H. Chen, H. Cheng, J. Wang and S. Tang, *Nano Energy*, 2021, **81**, 105609.
186 C. Zhang, H. Chen, X. Ding, F. Lorestani, C. Huang, B. Zhang, B. Zheng, J. Wang, H. Cheng and Y. Xu, *Appl. Phys. Rev.*, 2022, **9**, 011413.
187 J. Xu, Y. Li, F. Wang, W. Li, J. Zhan, S. Deng, C. Song, H. Yang, R. Cai and W. Tan, *Nano Lett.*, 2025, **25**, 2968–2977.
188 J. Tu, J. Min, Y. Song, C. Xu, J. Li, J. Moore, J. Hanson, E. Hu, T. Parimon, T. Y. Wang, E. Davoodi, T. F. Chou, P. Chen, J. J. Hsu, H. B. Rossiter and W. Gao, *Nat. Biomed. Eng.*, 2023, **7**, 1293–1306.
189 Y. Huang, H. Zhong, R. Yang, Y. Pan, J. Lin, C. K. W. Lee, S. Chen, M. Tan, X. Lu, W. Y. Poon, Q. Yuan and M. G. Li, *Biosens. Bioelectron.*, 2024, **259**, 116386.
190 Y. Lu, G. Yang, S. Wang, Y. Zhang, Y. Jian, L. He, T. Yu, H. Luo, D. Kong, Y. Xianyu, B. Liang, T. Liu, X. Ouyang, J. Yu, X. Hu, H. Yang, Z. Gu, W. Huang and K. Xu, *Nat. Electron.*, 2023, **7**, 51–65.
191 W. Babatain, U. Buttner, N. El-Atab and M. M. Hussain, *ACS Nano*, 2022, **16**, 20305–20317.
192 L. Yang, X. Chen, A. Dutta, H. Zhang, Z. Wang, M. Xin, S. Du, G. Xu and H. Cheng, *Nat. Commun.*, 2025, **16**, 792.
193 C. Paeng, A. Shanmugasundaram, G. We, T. Kim, J. Park, D.-W. Lee and C. Yim, *ACS Appl. Nano Mater.*, 2024, **7**, 4772–4783.
194 R. Murray, A. Muriqi, C. Larrigy, A. Russo, M. T. Mengistu, D. Iacopino, C. Fitzpatrick, M. Nolan and A. J. Quinn, *ACS Sustainable Chem. Eng.*, 2024, **12**, 15063–15076.
195 W. Lu, S. Xue, X. Liu, C. Bao and H. Shi, *Microchem. J.*, 2024, **196**, 109606.
196 W. Lu, Y. Wang, S. Liu, W. Xie, M. Wei and R. Hao, *Anal. Chim. Acta*, 2025, **1344**, 343715.
197 M. Pandey, M. Bhaiyya, P. Rewatkar, J. B. Zalke, N. P. Narkhede and H. Haick, *Adv. Healthcare Mater.*, 2025, **14**, e2500400.

